FEDERATED MRI RECONSTRUCTION WITH DEEP GENERATIVE MODELS

A THESIS SUBMITTED TO
THE GRADUATE SCHOOL OF ENGINEERING AND SCIENCE
OF BILKENT UNIVERSITY
IN PARTIAL FULFILLMENT OF THE REQUIREMENTS FOR
THE DEGREE OF
MASTER OF SCIENCE
IN
ELECTRICAL AND ELECTRONICS ENGINEERING

By
Gökberk Elmas
July 2023

Federated MRI Reconstruction with Deep Generative Models
By Gökberk Elmas
July 2023

We certify that we have read this thesis and that in our opinion it is fully adequate, in scope and in quality, as a thesis for the degree of Master of Science.

Tolga Çukur(Advisor)

Emine Ülkü Sarıtaş Çukur

Esin Öztürk Işık

Approved for the Graduate School of Engineering and Science:

Orhan Arıkan
Director of the Graduate School

ABSTRACT

FEDERATED MRI RECONSTRUCTION WITH DEEP GENERATIVE MODELS

Gökberk Elmas
M.S. in Electrical and Electronics Engineering
Advisor: Tolga Çukur
July 2023

Multi-institutional efforts can facilitate training of deep MRI reconstruction models, albeit privacy risks arise during cross-site sharing of imaging data. Federated learning (FL) has recently been introduced to address privacy concerns by enabling distributed training without transfer of imaging data. Existing FL methods employ conditional reconstruction models to map from undersampled to fully-sampled acquisitions via explicit knowledge of the accelerated imaging operator. Since conditional models generalize poorly across different acceleration rates or sampling densities, imaging operators must be fixed between training and testing, and they are typically matched across sites. To improve patient privacy, performance and flexibility in multi-site collaborations, here we introduce Federated learning of Generative IMage Priors (FedGIMP) for MRI reconstruction. FedGIMP leverages a two-stage approach: cross-site learning of a generative MRI prior, and prior adaptation following injection of the imaging operator. The global MRI prior is learned via an unconditional adversarial model that synthesizes high-quality MR images based on latent variables. A novel mapper subnetwork produces site-specific latents to maintain specificity in the prior. During inference, the prior is first combined with subject-specific imaging operators to enable reconstruction, and it is then adapted to individual cross-sections by minimizing a data-consistency loss. Comprehensive experiments on multi-institutional datasets clearly demonstrate enhanced performance of FedGIMP against both centralized and FL methods based on conditional models.

Keywords: MRI, accelerated, reconstruction, generative, prior, federated learning, distributed, collaborative.

ÖZET

DERİN ÜRETKEN MODELLER İLE FEDERE MRG REKONSTRÜKSIYONU

Gökberk Elmas
Elektrik Elektronik Mühendisliği, Yüksek Lisans
Tez Danışmanı: Tolga Çukur
Temmuz 2023

Çok kurumlu çabalar, görüntüleme verilerinin tesisler arası paylaşımı sırasında ortaya çıkan gizlilik risklerine rağmen derin MRG rekonstrüksiyon modellerinin eğitimini kolaylaştırabilir. Son zamanlarda gizlilik endişelerine yanıt olarak sunulan Federe Öğrenme (FÖ), görüntüleme verileri aktarılmaksızın dağıtık model eğitimini mümkün kılmaktadır. Mevcut FÖ yöntemleri, hızlandırılmış görüntüleme operatörünün açık bilgisini kullanarak, eksik örneklemeyle tam örnekleme arasında koşullu rekonstrüksiyon modellerini kullanır. Koşullu modeller, farklı hızlanma oranları veya örnekleme yoğunlukları arasında genelleme yapamadıklarından, görüntüleme operatörleri eğitim ve test arasında sabitlenmeli ve genellikle tesisler arasında eşleştirilmelidir. Hasta gizliliğini korumak, rekonstrüksiyon performansını ve çoklu tesis işbirliklerinde esnekliği arttırmak için, MRG rekonstrüksiyonunda üretken görüntü önselinin federe öğrenilmesi (FedGIMP) tanıtıyoruz. FedGIMP, iki aşamalı bir yaklaşım kullanır: üretken bir MRG önselinin tesisler arası öğrenmesi ve görüntüleme operatörünün enjekte edilmesinden sonra önsel uyarlaması. Global MRG önseli, latent değişkenlere dayalı koşulsuz bir çekişmeli modelle yüksek kaliteli MR görüntüleri sentezleyecek şekilde eğitilir. Yeni bir haritalayıcı alt ağı, önselde özgünlüğü korumak için tesise özgü latent değişkenler üretir. Çıkarım sırasında, önsel önce öznel örnekleme operatörleriyle birleştirilir ve rekonstrüksiyonu mümkün kılar, ardından veri tutarlılık kaybını en aza indirecek şekilde tekil çapraz kesitlere göre optimize edilir. Çoklu kurumsal veri kümelerinde yapılan kapsamlı deneyler, FedGIMP'in, koşullu modellere dayalı hem merkezi hem de FÖ yöntemlerine göre önemli ölçüde performansın artışı sağladığını göstermektedir.

Anahtar sözcükler: MRG, hızlandırılmış, rekonstrüksiyon, üretken, önsel, federe öğrenme, dağıtık, ortak.

Acknowledgement

To begin with, I want to express my gratitude to my advisor, Doç. Dr. Tolga Çukur, for his tireless support and guidance during my master's studies. His unwavering commitment to achieving excellence has motivated me to push myself beyond my limits and believe in my abilities. He has taught me that the most challenging and seemingly unsolvable problems often have the most intelligent and satisfying solutions, and his approach will undoubtedly shape my future career.

I would also like to acknowledge the members of the ICON Lab, including Atakan, Muzaffer, Mahmut, Onat, Şaban, and Yılmaz, for creating a nurturing academic environment and a friendly workplace. However, I must extend my warmest regards to Salman, whom I consider my second advisor, for his guidance throughout the development of this thesis.

As a part-time graduate student, I have dedicated most of my time to working for Aselsan Healthcare Systems, whose vision inspired me to move to Ankara and pursue my master's degree. I am committed to applying the results of my research to the development of medical imaging devices that will shape the future. I would also like to thank my colleagues in the Aselsan Healthcare System Engineering Department, including Erdem, who has been an incredibly supportive team leader, Önder, who has been a mentor to me in both work and life, Alper, my first Bilkenter friend, Doğukan, who has always been a calming presence in times of crisis, and Osman, who has shared in the hard work alongside me.

Finally, I must express my gratitude to my family, who have supported me in every decision I have made and sacrificed so much to help me become who I am today. It is my honor to dedicate this thesis to them as a tribute to their efforts.

Contents

List of Figures

List of Tables

Chapter 1

The content covered in this thesis are derived from the following publications:

- G. Elmas et al., "Federated Learning of Generative Image Priors for MRI Reconstruction," in IEEE Transactions on Medical Imaging, 2022, doi: 10.1109/TMI.2022.3220757.
- G. Elmas, S. U. Dar, Y. Korkmaz, M. Ozbey, and T. Çukur, "Federated MRI Reconstruction with Deep Generative Models," in Proceedings of ISMRM, 2023

Introduction

Magnetic Resonance Imaging (MRI) is a principal radiological modality owing to its non-invasiveness and exceptional soft-tissue contrast. Yet, an inevitable consequence of its low signal-to-noise ratio (SNR) efficiency is prolonged exams that hinder clinical use. Accelerated MRI methods based on undersampled acquisitions improve efficiency by recovering missing data via reconstruction algorithms that incorporate additional prior information [1, 2]. Deep learning models have been adopted for MRI reconstruction, given their strong ability to capture data-driven priors for inverse problems [3–46]. Deep reconstruction models are typically trained to perform a conditional mapping from undersampled acquisitions

to images that are consistent with respective fully-sampled acquisitions [47–55]. Since these models typically show poor generalization to features scarcely present in the training set, learning of generalizable models involves training on a large and diverse collection of MRI data [56]. Unfortunately, economic and labor costs along with patient privacy concerns can prohibit compilation of comprehensive datasets centralized at a single institution [57].

Aiming at this limitation, federated learning (FL) is a promising framework that facilitates multi-institutional collaborations via decentralized training of learning-based models [58–63]. An FL server periodically collects locally-trained models from individual sites in order to obtain a shared global model across sites [64, 65]. Following aggregation of local models, the global model is then broadcast back onto individual sites for continual training. This decentralized procedure allows a multi-site model to be collaboratively trained without sharing of local data, thereby mitigating privacy concerns [66]. A multi-site model can improve generalization over single-site models given the native diversity in multi-institutional data, which can substantially benefit sites with relatively limited or uniform training data. However, this comes at the potential expense of lower site-specific performance due to data heterogeneity across sites, lowering sensitivity to site-specific image features particularly for non-adaptive architectures that are vulnerable to domain shifts [62, 67].

Characteristics of acquired data are governed by two extrinsic factors in the context of accelerated MRI. At primary level, the spatial distribution of tissue magnetization (i.e., the MR image distribution) is determined by the pulse sequence and the scanner [56]. At secondary level, the MR image distribution is further modulated by the accelerated imaging operator, which captures the influences of undersampling in k-space and reception by coil arrays [68]. As such, multi-site MRI data can show substantial heterogeneity in the MR image distribution (e.g., due to different sequences, scanners) or the imaging operator (e.g., due to different acceleration rates, sampling densities). In turn, multi-site models can suffer from performance losses under significant domain shifts across sites, or across the training and test sets [63, 69].

Few recent studies on FL-based MRI reconstruction have considered domain shifts across sites. In [70], adversarial alignment between source and target sites was proposed to improve similarity of latent-space representations in reconstruction models. In [71], reconstruction models were split into a global encoder shared across sites, followed by local decoders trained separately at each site. Despite improved performance against across-site variability, both methods are based on conditional models that assume explicit knowledge of the imaging operator. Conditional models generalize poorly under changes to the imaging operator [72, 73]. In turn, matching acceleration rates and sampling densities must be prescribed between the training and test sets, and similar prescriptions are often utilized among sites [70]. This requirement can restrict flexibility in multi-institutional collaborations and necessitate model retraining under significant changes to the desired imaging operator [69].

Contributions

In this thesis, we introduce a novel FL method for MRI reconstruction, FedGIMP, to enhance patient privacy, performance and flexibility in multi-site collaborations. Unlike previous FL methods, we propose a two-stage reconstruction approach: cross-site training of a generative MRI prior that captures the MR image distribution (Fig. 3.1), and prior adaptation following injection of the subject-specific imaging operator (Fig. 3.2). To improve generalization, we train a global MRI prior operationalized as an unconditional adversarial model that synthesizes high-quality MR images. Training images are derived from coil-combined, fully-sampled acquisitions to decouple the influence of the imaging operator from the prior. The statistics of feature maps across the synthesizer are controlled by latent variables produced by a mapper. To improve specificity, we propose a novel mapper that produces site-specific latents given a site index. During inference, the global MRI prior is combined with subject-specific imaging operators that can vary flexibly across sites and between the training and test sets. Reconstruction is then performed by adapting the MRI prior to enforce consistency between

synthesized and acquired k-space data. This adaptation further boosts site specificity by increasing conformity of the multi-site model to the distribution of test data.

- We introduce a novel FL method for MRI reconstruction that decentrally trains a generative MRI prior decoupled from the imaging operator to improve patient privacy and flexibility in multi-site collaborations.
- We operationalize the prior as an unconditional adversarial model with a cross-site-shared generator to capture site-general representations, albeit with site-specific latents to maintain specificity in synthesized MR images.
- We leverage prior adaptation to enhance specificity of the multi-site model and improve reliability against domain shifts across sites and across training and test sets.

Related Work

Deep MRI reconstruction is pervasively based on conditional models that directly map undersampled acquisitions to images consistent with fully-sampled acquisitions [4]. These models are trained on large sets of paired input-output data under a specific accelerated imaging operator. Heavy data demand limits applicability since curating large datasets at a single site is challenging [74, 75]. To facilitate curation, unpaired [49, 76, 77], self-supervised [78–83], or transfer [6, 69] learning strategies were proposed. However, these methods require centralized training following cross-site data transfer that raises patient privacy concerns [57].

FL is a decentralized framework for multi-institutional collaborations that communicates model parameters instead of raw data [66]. FL distributes costs related to the formation and processing of datasets across sites, while mitigating concerns regarding the data privacy [57]. FL methods have readily been demonstrated on imaging tasks such as segmentation and classification [58, 59, 61]. A

major consideration is the reliability against domain shifts in multi-site imaging data, collected with varying imaging protocols and scanners. Data harmonization was proposed to remove site-specific variations while emphasizing shared variability across sites [84–86]. Although harmonization can improve population-level analysis, it can discard patient-level information of diagnostic value. Episodic learning in frequency space was proposed to improve generalization to unseen test domains for segmentation [63]. Adversarial alignment and network splitting methods were also proposed for classification [62, 87, 88]. While promising results were reported, it is nontrivial to directly adopt image analysis models for MRI reconstruction that requires image formation from raw data.

Domain shifts in MRI reconstruction involve heterogeneity in the MR image distribution and in the imaging operator, which can elicit performance losses when heterogeneity is prominent across sites, or across the training-test sets [69]. Few recent FL studies on single-coil MRI reconstruction have considered domain shifts across sites. In [70], cross-site-shared latent-space representations were obtained by adversarially aligning all sites to the targeted test site in each communication round. In [71], a split reconstruction model with a global encoder and unshared decoder was used to maintain site-specific and site-general representations. While demonstrating remarkable results, these recent methods are based on conditional models that are explicitly informed on the imaging operator. This can limit reconstruction performance and necessitate model retraining under notable domain shifts in the imaging operator [72, 73]. As such, previous studies have prescribed matching acceleration rates and sampling densities between the training-test sets, and usually across sites.

Here, we propose an FL method that learns a generative MRI prior, and reconstructs images via prior adaptation after combination with the subject-specific imaging operator. Separation of the MRI prior from the imaging operator has recently been considered for centralized reconstruction models trained on single-site data [67, 89, 90], yet it has not been studied in the context of FL. To our knowledge, FedGIMP is the first FL method that decouples the MRI prior from the imaging operator to train decentralized reconstruction models on multi-site

datasets, and the first FL method that reconstructs multi-coil MRI data. Furthermore, FedGIMP includes several unique design elements compared to previous centralized methods. In [89], a non-adaptive MRI prior was proposed that was kept static during inference. In [67], an adaptive MRI prior was proposed that did not include latents, so no latent optimization was performed during inference. In [90], an adaptive MRI prior was proposed that included mapper-produced latents albeit no site index, and the mapper was removed from the prior to directly optimize latents during inference. Unlike previous methods, FedGIMP introduces a novel site-index in its adaptive MRI prior to maintain site specificity, and it updates the mapper to indirectly optimize latents. These unique aspects enable FedGIMP to offer improved performance for MRI reconstruction on heterogeneous datasets.

Outline

The extend of the rest of this thesis is as follows. Second and third chapters contain introductory level information on accelerated MRI reconstruction and federated learning. Forth chapter covers the theory behind the proposal model. Fifth chapter is about the architectural details of the proposed model, competing models, conducted experiments and how they are evaluated metrically. Sixth chapter depicts the visual and metric experimental results under different test scenarios. Seventh chapter is devoted for the discussions of the results covered in chapter six, and followed by a conclusive eigthth chapter. Tables and Figures can be found at the relevant locations throughout the text.

Chapter 2

Magnetic Resonence Imaging

Magnetic Resonance Imaging (MRI) uses a combination of magnetic field and radio-frequency pulses to excite and align hydrogen nuclei (1H) in the human body. The hydrogen nuclei are aligned by a strong external magnetic field, while a sequence of radio-frequency pulses excites the protons in the transverse direction. Changes in magnetic flux captured by receiver coils as these excited protons relax, are stored as raw data known as k-space, which is a data matrix containing spatial frequency information of the target MR image. Higher spatial frequency components of the image correspond to the outer rows of the data matrix, while the lower spatial frequency components are encoded in the inner rows. The relationship between k-space and the image domain is established using Fourier transform.(Figure 2.1.a)

Accelerated MRI Reconstruction

MRI provides excellent soft-tissue contrast, but long scan duration limits its usage, especially in emergency cases [91]. Therefore, accelerating MRI while maintaining high image quality is an area of active research. Various techniques, such as parallel imaging, compressed sensing, simultaneous multiple slice imaging, and

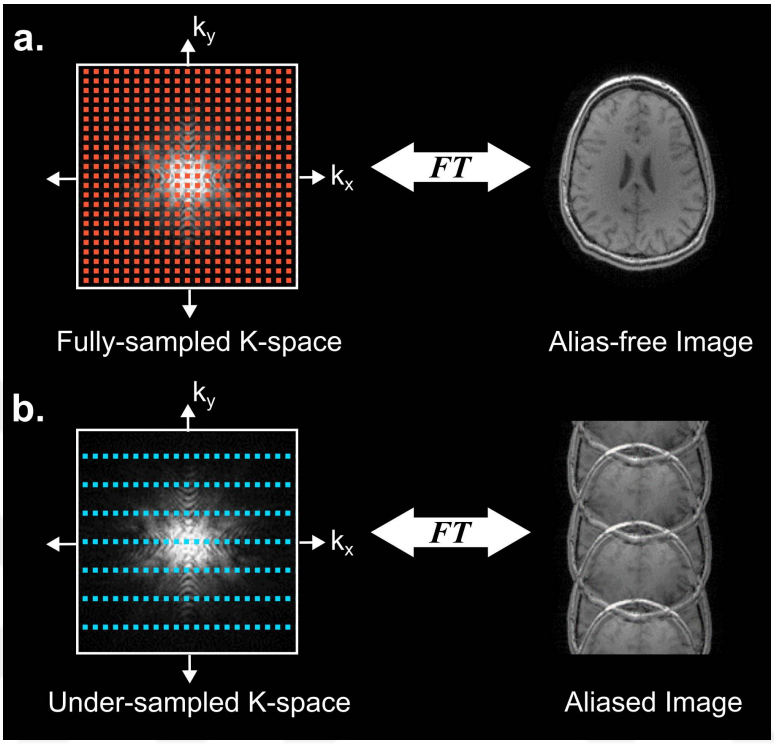

Figure 2.1: There is a Fourier-relation between raw data and MR image in spatial domain. If k-space is sampled above Nyquist rate, reconstrcted image does not suffer from aliasing artifacts (a). Accelerated MRI scans involves under-sampling of k-space so that aliasing occurs in spatial domain with respect to the undersampling operator (b).

ultra-fast sequences, have been proposed to accelerate MRI [92–129]. Parallel imaging, in particular, is a robust method that uses an array of spatially sensitive independent receiver coils to form a high-quality image from fewer k-space samples.

Despite the benefits of MRI acceleration techniques, each method introduces specific artifacts in the reconstructed image, primarily due to aliasing in the spatial domain (Figure 2.1.b). The primary objective of MRI acceleration is to extract maximum detail from the undersampled raw data to create a high-quality image.

A typical accelerated scan of multiple imaging coils can be formulated as:

$$F_P C m = y \tag{2.1}$$

where F_P is the partial Fourier operator defined by acceleration pattern/rate and

scanner specific parameters, C stands for coil sensitivity maps, m signifies MR image to be reconstructed, and y denotes the raw k-space data. The Equation 2.1 can be refined as:

$$Am = y \tag{2.2}$$

where A is the imaging operator combining all the factors covered by F_P and C. Reconstructing the resultant image m from the raw data contained in y is an underdetermined problem, so a prior information of m is required to get a high quality image. Thus, we can update Equation 2.2 as:

$$\widehat{m} = \underset{m}{\operatorname{argmin}} \|y - Am\|_2^2 + H(m), \tag{2.3}$$

where $\widehat{m}$ is the reconstructed image and $H(m)$ is a regularization term. $H(m)$ could represent the sparsity prior [130, 131] in undersampling scheme, structural low-rank priors [132–135], or deep learning based priors [12,22,26,136–141]. Deep neural networks are traditionally trained in supervised fashion, where undersampled and fully sampled images are fed to the network as pairs. During the training stage, network parameters are optimized to minimize the following loss function:

$$\mathcal{L}(\theta) = \|G(m_{us}^i; \theta) - m_{fs}^i\|_p \tag{2.4}$$

where m_{us}^i and m_{fs}^i are under- and fully-sampled image pair with i^{th} index, $G(.;\theta)$ is the image generation network given the trained network weights θ, $\|.\|_p$ is the norm function of $\mathcal{L}^p$ distance. Inference stage uses the prior information learnt in offline training session to reconstruct fully-sampled images of given under-sampled test images, which can be formulated as:

$$\widehat{m} = \underset{m}{\operatorname{argmin}} \|y - Am\|_2^2 + \beta \|G(m_{us}; \widehat{\theta}) - m\|_p \tag{2.5}$$

where β is regularization strength of deep neural network, $G(m_{us}; \widehat{\theta})$ is the network output for under-sampled input m_{us} given the learnt weights $\widehat{\theta}$. Although the training procedure is an offline separate session, the learnt prior does not have to be static. Recent Deep Image Prior (DIP) methods have shown that even untrained, randomly initialized deep neural networks could be used as native image regularizes with a test sample specific optimization. A DIP optimization can be formulated as the following minimization problem:

$$\theta^* = \underset{\theta}{\operatorname{argmin}} \|AG(z;\theta) - y\|_p \tag{2.6}$$

where θ are randomly initialized network parameters to optimize and $G(z;\theta)$ is the generated image given latent variable z. Instead of random initialization, we can use learnt network weights to start inference from and formulate the training loss as:

$$\mathcal{L}(\theta) = \|G(z;\theta) - m^i_{fs}\|_p \tag{2.7}$$

where $G(z;\theta)$ is the generator network using a random latent variable z to synthesize fully sampled image m^i_{fs}. This training procedure allow us to generate other fake fully sampled images by changing the given random latent z. Thus, inference stage is about maintaining consistency between randomly generated image from the prior and under-sampled k-space points obtained from the test subject, which can be formulated as:

$$\widehat{m} = \underset{z,\theta^*}{\operatorname{argmin}} \|AG(z;\theta^*) - y_{us}\|_p \tag{2.8}$$

where $\widehat{m}$ is the reconstructed image, z is the input latent, θ^* is the learnt network weights of the prior, A is the combined operator for partial Fourier operator and coil sensitivities, $G(.;\theta^*)$ is the trained generator network synthesizing fake fully sampled images given a random latent z, y_{us} are under-sampled raw k-space data of a given test subject, and $\|.\|_p$ is the norm operator where p is typically 1 or 2.

The training scheme in Equation 2.7 and inference stage in Equation 2.8 have a major implication on the dependency to the partial Fourier operator contained in A. The offline training stage depicted in Equation 2.5 depends to the undersampling pattern, and scanner/coil characteristics inherited in m_{us}, thus the deep neural network trained in this manner is conditioned to the exact imaging operator. Unlike Equation 2.5, a generator network trained with the loss function in Equation 2.7 is independent from the imaging operator and only learns prior information about fully-sampled MR images. The exact imaging operator is injected during inference stage (Equation 2.8), so the training is unconditional to imaging operator and the learnt prior can be flexibly adapted to any test subject specific case. Overall, unconditional prior training with inference optimization would have a fair generalization performance whilst maintaining test subject specificity in reconstructed image.

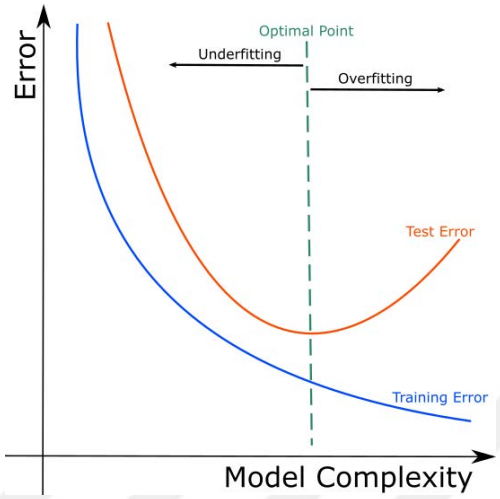

Figure 2.2: The model complexity allows researchers to solve more complex problems, but the lack of training data could lead to overfitting problem and the test performance of the trained model degrades.

Federated Learning

Deep learning methods' performance depend on two factors: the neural network model and the training data. From the most basic perspective, the complexity of the model allow the network to capture fine details and solve more complex problems whilst the data contains different variations in a source distribution from which we want to infer our task's results. Recent advances [142] in hardware allowed extremely complex models with millions of parameters to be trained in feasible time. From DenseNet [143] with almost 10 million parameters to vision transformers [144] with approximately 100 million parameters, computer vision literature has become diverse in neural network options. Complex problems with little-to-none solutions become a matter of a certain training time. For instance, a deep learning model can outperform expert physicians in chest x-ray analysis [145]. Yet the publicly available dataset are scarce and sharing certain personal data like medical images, has a huge privacy violation potential [146]. The scarcity of available training data is a bottleneck for up-to-date deep learning models [147]. The more complex the model, the more data the network needs. Limited training set leads over-fitting, and heavily degrades test performance due to loss of generality (Fig. 2.2).

Overfitting can be beaten by other approaches [148] like cross-validation, regularization, or data augmentation. However, these techniques limit the potential of the model, thus collecting more data is a must. Centralized training by data transfer from multiple sources has its-own problems. First of all, multiple data sites mean a huge variation in collected data. At first, this might seem why the data is collect in the first place, but some site specific parameters could disturb the learning process [149]. Consider different MRI scanners in different hospitals, whose magnetization uniformity, coil sensitivities, scanning sequences are different, even for the same body part scan. Sharing medical images might be quite dangerous. For instance, it is possible to reconstruct the original human face from brain MRI scans [150]. There is a huge patient privacy risk, and any responsible study on these data is bound to strict ethical and legal regulations. Federated Learning (FL) is proposed as a privacy-preserving multi-site collaboration effort that abides patient privacy needs. The goal of FL is to keep the training data locally, but enjoy the generalization performance. In any type of FL setting, the participating sites train a certain global model, that is shared across sites, for a certain amount of iterations. Then periodically, locally updated models are aggregated across sites. The aggregation can either be on an FL Server (Fig. 2.3), that is coordinating the collaboration process, or the sites may communicate with each other and update the global model in any one of the sites. The introduction of an FL Server is named as cross-silo FL where the exchange of the model is between each site and the FL Server, this setting also known to have low number of sites. Considering medical images are scarce and hospitals with only a handful of expert radiographers are the main supply of the data, most of the medical imaging application of FL uses cross-silo training scenario.

There have been many algorithms proposed on the aggregation of global models, but Federated Averaging (FedAVG) is the most common and one of the first FL algorithms. FedAVG has been proposed by Google, and has its basics on weighted averaging of model updates across sites. In the original paper [64], this aggregation strategy is shown to be performing equivalently to centralized training. Other variations of FedAVG [151] have been proposed to prevent any site's

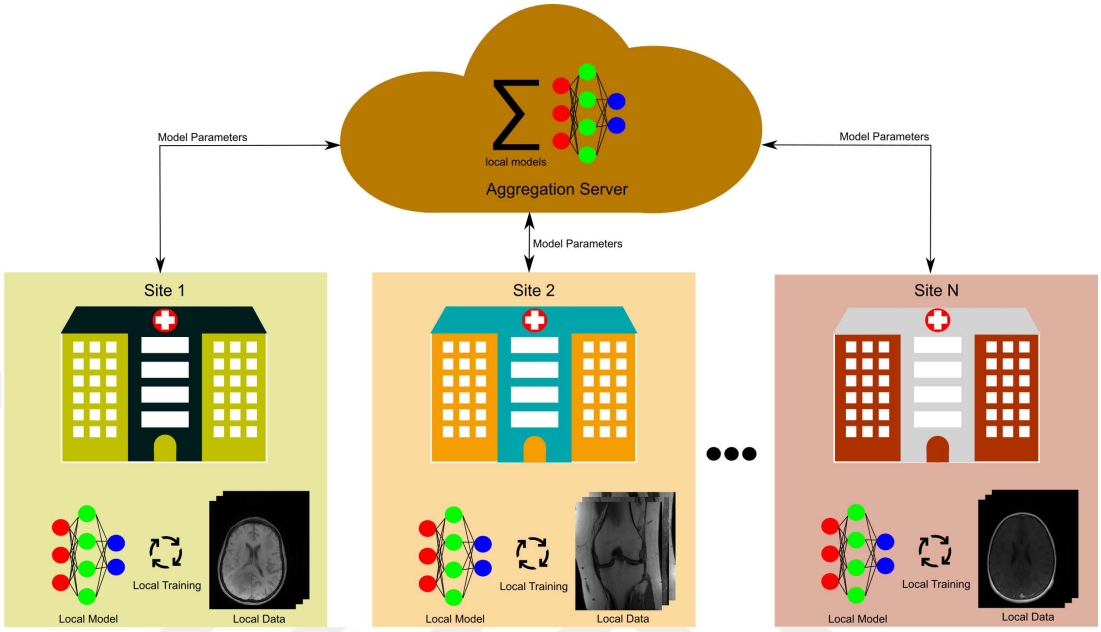

Figure 2.3: Cross-silo FL training includes a handful of data sites collaborating with an FL Server. Periodically, each site trains a local model with locally kept private data, and the updates model is shared with the FL Server for aggregation. This sequence is called a communication round and continues over time.

update to become too dominant and disturb the learning process such as gradient clipping and trainable averaging weights.

Chapter 3

Theory

3.1 Federated Learning of Conditional MRI Models

Accelerated MRI entails reconstruction of an underlying MR image m from undersampled k-space acquisitions y:

$$Am = y, \tag{3.1}$$

where A is the imaging operator that includes the effects of coil sensitivities and partial Fourier transformation on acquired k-space. As Eq. 3.1 is underdetermined, additional prior information is incorporated to regularize the reconstruction:

$$\widehat{m} = \underset{m}{\operatorname{argmin}} \|y - Am\|_2^2 + H(m), \tag{3.2}$$

where $H(m)$ enforces the prior [1]. Deep models have recently become the predominant method for solving Eq. 3.2 by training of data-driven priors on diverse datasets [4].

In FL, training is performed via communication between multiple sites and a server [66]. The server retains a global model (C_θ with parameters θ), whereas

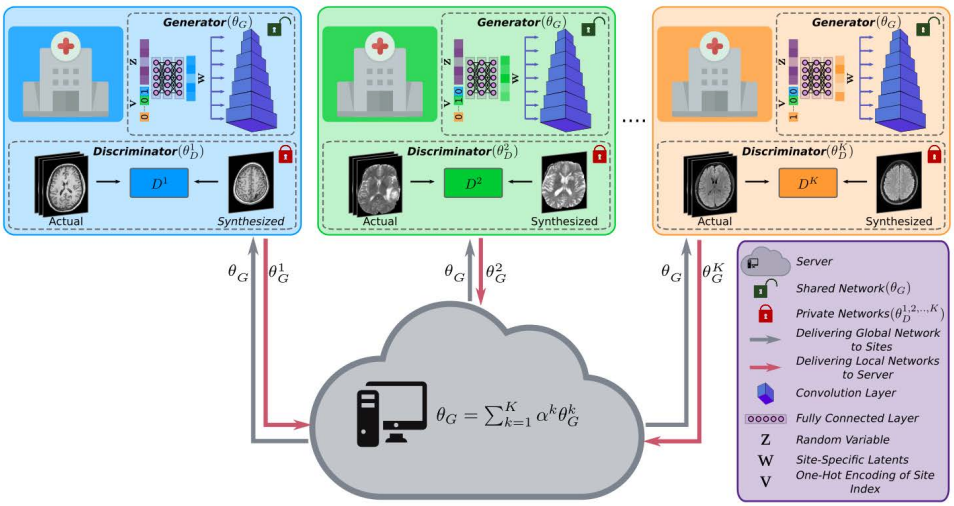

Figure 3.1: FedGIMP performs federated learning of a generative image prior for MRI reconstruction. The prior is embodied as an unconditional adversarial model that synthesizes high-quality MR images given site-specific latent variables. Cross-site-shared generators of parameters θ_G are used along with site-specific discriminators of parameters $\theta_D^{1,..,K}$. In each communication round, sites perform local updates to θ_G to minimize a synthesis loss, and the server then aggregates updated models.

each site retains a local model of matching architecture (C_θ^k for site k, where $k \in \{1, .., K\}$). In each communication round, local models are initialized with the global model broadcast from the server, $\theta_C^k \leftarrow \theta_C$, and updated to minimize a local reconstruction loss:

$$\mathcal{L}_{Rec}^k(\mathcal{D}^k, A_{tr}^k; \theta^k) = \mathbb{E}_{(m_{tr}^k, y_{tr}^k)} \left[\| m_{tr}^k - C_{\theta^k}(A_{tr}^{\dagger k} y_{tr}^k) \|_2 \right], \tag{3.3}$$

where $\mathbb{E}$ denotes expectation, $\mathcal{D}^k$ are local training data comprising undersampled acquisitions (y_{tr}^k) and reference images obtained from fully-sampled acquisitions (m_{tr}^k), and A_{tr}^k, $A_{tr}^{\dagger k}$ are the imaging operator and its adjoint. C is a conditional model with parameters θ^k that receives zero-filled Fourier reconstruction of y_{tr}^k. At the end of each round, updated local models are aggregated via federated averaging (FedAvg) [64]:

$$\theta = \sum_{k=1}^{K} \alpha^k \theta^k, \tag{3.4}$$

where α^k denotes the relative site weights.

The trained global model (C_{θ^*}) is then used for inference:

$$\hat{m}_{k,s} = C_{\theta^*}(A_{test}^{\dagger k} y_{test}^{k,s}), \tag{3.5}$$

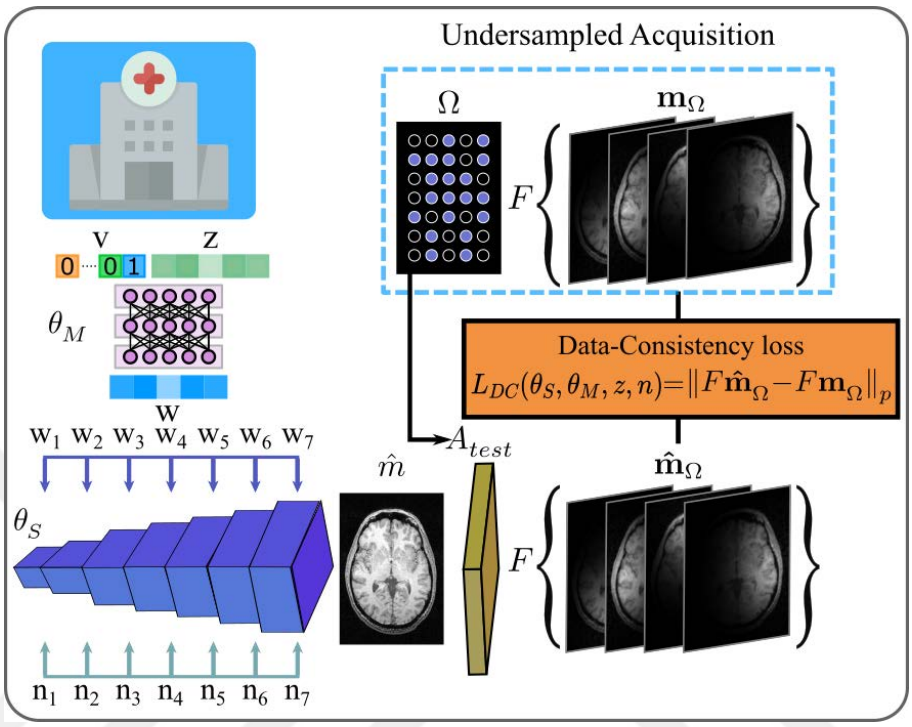

Figure 3.2: FedGIMP's MRI prior is embodied as a generator that synthesizes a high-quality, coil-combined MR image ($\hat{m}$). To perform reconstruction, the trained generator is combined with the subject-specific imaging operator at a test site (A_{test}) and adapted to minimize a data-consistency loss on acquired k-space samples (L_{DC}). L_{DC} is expressed by projecting $\hat{m}$ onto individual coils, undersampling multi-coil images in k-space (with the pattern Ω), and comparing synthesized and acquired k-space samples. For each cross-section, inference optimization is conducted over the synthesizer and mapper parameters ($\theta_{S,M}$), normal variables (z) and noise (n).

where $\hat{m}_{k,s}$ is the reconstruction and $y_{test}^{k,s}$ is the undersampled acquisition for the s^{th} subject at the k^{th} site, and $A_{test}^{\dagger k}$ is the adjoint imaging operator at site k. Since conditional models generalize poorly against heterogeneity in the imaging operator, A_{tr}^{k} and A_{test}^{k} are typically matched across training-test sets (i.e. across training and test subjects), and across sites.

3.2 Federated Learning of Generative MRI Priors

To improve flexibility in multi-site collaborations, we propose a novel FL method based on decentralized learning of generative MRI priors. A global MRI prior is trained using an unconditional adversarial model with shared generator and local discriminator networks (Fig. 3.1). During inference, the prior is combined with subject-specific imaging operators and adapted to the reconstruction task (Fig. 3.2). The proposed architecture and learning procedures are described below.

3.2.1 Unconditional Adversarial Model

FedGIMP employs an unconditional architecture to learn a generative prior for high-quality MR images. Training images are derived from coil-combined, fully-sampled acquisitions to obtain a prior that is agnostic to k-space undersampling and individual coil sensitivities. Here, we propose a style-generative model as inspired by the success of this model family in natural image synthesis [152]. Our proposed model has a generator that synthesizes realistic MR images, wherein the statistics of feature maps at each stage are controlled via latent variables. These statistics are expected to be different across sites given the native heterogeneity of MR images collected in separate sites. Our model introduces a novel mapper with a site index to produce site-specific latent variables, thereby increasing specificity in synthesized feature maps. Finally, a discriminator differentiates between synthetic and actual MR images.

Generator (G): The generator uses mapper (M) and synthesizer (S) sub-networks to transform low-dimensional random variables onto high-dimensional MR images. $\underline{M}$ receives i.i.d. normal variables $z \in \mathbb{R}^{1\times J}$ concatenated with a one-hot encoding vector for site index $v \in \mathbb{R}^{1\times K}$. Given an input in $\mathbb{R}^{1\times(J+K)}$, it computes latent variables $w \in \mathbb{R}^{1\times J}$:

$$w = M_{\theta_M}(z \oplus v), \tag{3.6}$$

where $\oplus$ denotes concatenation. At the i^{th} layer of M with L_M layers, latent variables z_i are mapped onto z_{i+1} as:

$$z_{i+1} = FC_{M,i}(z_i), \tag{3.7}$$

where $FC_{M,i}$ is a fully-connected layer with parameters $\theta_{M,i} \in \mathbb{R}^{(J+K)\times J}$ if $i = 1; \mathbb{R}^{J\times J}$ if $i \neq 1$. Dimensionality is reduced from $J + K$ to J in the first layer, and retained in remaining layers. Receiving w from M, $\underline{S}$ generates an MR image progressively across L_S layers. In the i^{th} layer, feature maps from the preceding layer ($X_i^0 \in \mathbb{R}^{\frac{h_1}{2}\times\frac{h_2}{2}\times q}$) are two-fold upsampled. The upsampled maps ($X_i^1 \in \mathbb{R}^{h_1\times h_2\times q}$) are then processed through a cascade of blocks: $Conv_S^1$ (convolution), NI^1 (noise injection), $AdaIN^1$ (adaptive instance normalization), $Conv_S^2$, NI^2, $AdaIN^2$. The first block extracts local features, $X_i^2 = Conv_S^1(X_i^1)$:

$$X_i^2 = \begin{bmatrix} \sum_c X_i^{1,c} \circledast \theta_{S,i}^{c,1} \\ \vdots \\ \sum_c X_i^{1,c} \circledast \theta_{S,i}^{c,u} \end{bmatrix}, \tag{3.8}$$

where $\theta_{S,i}^1 \in \mathbb{R}^{j\times j\times q\times u}$ are convolution kernels, u is the number of output feature channels, c is the channel index, and $\circledast$ denotes convolution. In Eq. 3.8, X_i^2 is a 3D tensor and matrix rows span the 3^{rd} dimension of X_i^2. Next, the noise-injection block introduces pixel-level intensity modulations in the feature maps. Recent computer vision studies have reported that introducing noise variables across the synthesizer improves details in synthetic natural images [152]. Accordingly, scaled noise variables are added onto feature maps to control low-level structural details, $X_i^3 = NI^1(X_i^2)$:

$$X_i^3 = \begin{bmatrix} \varphi(X_i^{2,1} + \epsilon_i^{1,1} n_i^1 \\ \vdots \\ \varphi(X_i^{2,u} + \epsilon_i^{1,u} n_i^1) \end{bmatrix}, \tag{3.9}$$

where $n_i^1 \in \mathbb{R}^{h_1\times h_2}$ is multiplied with the scalar $\epsilon_i^{1,c}$ and added onto the c^{th} channel of $X_i^2 \in \mathbb{R}^{h_1\times h_2\times u}$, φ is an activation function. To control high-level style

features, adaptive instance normalization modulates feature maps given intermediate latent variables, $X_i^4 = AdaIN^1(X_i^3, w)$ [153]:

$$X_i^4 = \gamma_i^1(w)\frac{(X_i^3 - \mu(X_i^3))}{\sigma(X_i^3)} + \beta_i^1(w), \tag{3.10}$$

where $\gamma_i^1 \in \mathbb{R}^{u\times 1}$ and $\beta_i^1 \in \mathbb{R}^{u\times 1}$ are learnable affine transformations of w that control the scale and bias of each feature channel respectively. μ and σ are mean and variance along the channel dimension of X_i^3. Note that the cascade of convolution, noise injection and adaptive instance normalization is repeated a second time to yield the mappings $X_i^5 = Conv_S^2(X_i^4)$, $X_i^6 = NI^2(X_i^5)$, $X_{i+1}^0 = AdaIN^2(X_i^6, w)$. The parameters of these repeat blocks are distinct from those in the initial blocks, except for tied intermediate latents input to $AdaIN^{1,2}$. Overall, the mapping through the generator is:

$$\hat{x} = G_{\theta_G}(z \oplus v, n) = S_{\theta_S}(M_{\theta_M}(z \oplus v), n), \tag{3.11}$$

where $\hat{x}$ is the synthesized image, the generator parameters θ_G=$\{\theta_M, \theta_S\}$ include mapper and synthesizer parameters.

Discriminator (D): The discriminator attempts to discriminate between actual or synthetic MR image inputs. D contains $L_D - 1$ layers cascading two-fold downsampling and convolution blocks ($Conv_D$), followed by a final fully-connected layer (FC_D). The overall mapping is:

$$x_D = D_{\theta_D}(x), \tag{3.12}$$

where x is an actual (x_r) or synthetic image ($\hat{x}$), $x_D \in \mathbb{R}^1$ is the output, and D_{θ_D} is parametrized by θ_D.

3.2.2 Training of the Global MRI Prior

To learn a global MRI prior, FedGIMP performs federated training of the unconditional adversarial model (Alg. 1). The training lasts a total of L communication rounds between the sites and the server. A shared generator (G) and K local generator copies (G^k) are maintained. Meanwhile, K local discriminators (D^k)

Algorithm 1: FedGIMP training

Input: $\mathcal{D} = \{\mathcal{D}^1, ..., \mathcal{D}^K\}$: datasets from K sites.
L: number of communication rounds.
I: number of local epochs.
$\{G^1, ..., G^K\}$: local generators of params. $\{\theta_G^1, ..., \theta_G^K\}$.
$\{D^1, ..., D^K\}$: local discriminators of params. $\{\theta_D^1, ..., \theta_D^K\}$.
$\{\alpha^1, ..., \alpha^K\}$: weighting coefficients of K sites.
G: global generator of params. θ_G.
$Opt()$: optimizer that computes parameter updates.
Output: G trained global model of params. θ_G^*.

Initialize parameters
for $l = 1 : L$ **do**
  for $k = 1 : K$ **do**
    $\theta_G^k \leftarrow \theta_G$ (receive global generator)
    for $i = 1 : I$ **do**
      Calculate $\nabla_{\theta_G^k} \mathcal{L}_G^k(\theta_G^k)$
      $\theta_G^k \leftarrow \theta_G^k - Opt(\nabla_{\theta_G^k} \mathcal{L}_G^k)$
      Calculate $\nabla_{\theta_D^k} \mathcal{L}_D^k(\mathcal{D}_i^k; \theta_D^k)$
      $\theta_D^k \leftarrow \theta_D^k - Opt(\nabla_{\theta_D^k} \mathcal{L}_D^k)$
  $\theta_G \leftarrow \sum_{k=1}^K \alpha^k \theta_G^k$ (aggregate local generators)
return $\theta_G^* = \theta_G$

are not exchanged to limit communication load and augment data privacy. In the first round, G and D^k are randomly initialized. At the start of each round, local generators are initialized with the global generator broadcast from the server, $\theta_G^k \leftarrow \theta_G$. In each round, I local epochs are performed to update local models. The local generator updates are calculated to minimize a non-saturated logistic adversarial loss (L_G^k):

$$L_G^k(\theta_G^k) = -\mathbb{E}_{p(z)} \left[\log(f(D^k(G_{\theta_G^k}^k(z \oplus v, n)) \right], \tag{3.13}$$

where $\mathbb{E}_{p(.)}$ is expectation with respect to probability distribution p. The local discriminator updates are calculated to also minimize a non-saturated logistic adversarial loss (L_D^k), along with a gradient penalty according to the learned

Algorithm 2: FedGIMP inference

Input: $y_{test}^{k,s}$: Undersampled data for k^{th} site, s^{th} subject.
$A_{test}^{k,s}$: subject-specific imaging operator for $y_{test}^{k,s}$.
$G = \{M, S\}$: global generator with params. $\theta_G^* = \{\theta_M^*, \theta_S^*\}$.
v: site-specific one-hot encoding vector.
z: i.i.d normal variable.
E: number of iterations for inference.
Output: $\hat{m}_{k,s}$: reconstructed image.

$\theta_S^1 \leftarrow \theta_S^*$, $\theta_M^1 \leftarrow \theta_M^*$, $z^1 \leftarrow z$
for $e = 1 : E$ **do**
  Calculate $\nabla_{\theta_S^e, \theta_M^e, z^e} \mathcal{L}_{DC}^{k,s}(y_{test}^{k,s}, A_{test}^{k,s}; \theta_S^e, \theta_M^e, z^e)$
  $\theta_S^{e+1} \leftarrow \theta_S^e - Opt(\nabla_{\theta_S^e} \mathcal{L}_{DC}^{k,s})$
  $\theta_M^{e+1} \leftarrow w^e - Opt(\nabla_{\theta_M^e} \mathcal{L}_{DC}^{k,s})$
  $z^{e+1} \leftarrow z^e - Opt(\nabla_{z^e} \mathcal{L}_{DC}^{k,s})$
$\hat{m}_{k,s} = S_{\theta_S^E}(M_{\theta_M^E}(z^E \oplus v))$
return $\hat{m}_{k,s}$

distribution of actual MR images $p(x_r^k)$ [152]:

$$\begin{aligned} L_D^k(\mathcal{D}^k; \theta_D^k) = &- \mathbb{E}_{p(z)} \left[\log(1 - f(D_{\theta_D^k}^k(G(z \oplus v, n)))) \right] \\ &- \mathbb{E}_{p(x_r^k)} \left[\log(f(D_{\theta_D^k}^k(x_r^k)) \right] \\ &+ \frac{\delta}{2} \mathbb{E}_{p(x_r^k)} \left[\left\| \nabla D_{\theta_D^k}^k(x_r^k) \right\|^2 \right], \end{aligned} \tag{3.14}$$

where $\mathcal{D}^k$ are training data from site k, i.e. coil-combined MR images derived from fully-sampled acquisitions (x_r^k). After I iterations of updates according to Eqs. 3.13 and 3.14, local generators are sent to the server for aggregation [64]:

$$\theta_G = \sum_{k=1}^{K} \alpha^k \theta_G^k \tag{3.15}$$

Here, α^k is set to $\frac{N^k}{N}$, where N is the total number of training samples across all sites and N^k is the number of training samples at the k^{th} site.

3.2.3 Inference at a Test Site

FedGIMP trains an unconditional prior that randomly generates high-quality, coil-combined, synthetic MR images. Synthetic images do not carry information on coil sensitivities or k-space sampling patterns, and they lack anatomical correspondence to the actual subject. Thus, a dedicated inference procedure is required for reconstruction. Synthetic images define a constraint reflecting the learned image distribution, whereas the subject's undersampled acquisitions define an anatomical constraint in accordance with the imaging operator. The two constraints do not necessarily have an intersection (e.g., a prior trained on brain images used to reconstruct knee images). For reconstruction, FedGIMP adapts its prior to refine the associated constraint and intersect it with the anatomical constraint. This adaptation enforces the prior to generate an image whose undersampled k-space data matches acquired data.

During inference, FedGIMP first combines the trained MRI prior with the subject-specific imaging operator at a test site ($A_{test}^{k,s}$). To do this, the prior can be included in the optimization problem for various model-based reconstructions [8, 9, 48, 154]. Here, we follow a straightforward approach where the prior is adapted to minimize a data-consistency loss between synthesized and acquired k-space data (Alg. 2):

$$L_{DC}^{k,s}(y_{test}^{k,s}, A_{test}^{k,s}; \theta_S, \theta_M, z, n) = \left\| A_{test}^{k,s} S_{\theta_S}(w, n) - y_{test}^{k,s} \right\|_2 + \eta \left\| \nabla S_{\theta_S}(w, n) \right\|, \tag{3.16}$$

where $w = M_{\theta_M}(z \oplus v)$, and a gradient penalty is included with weight η to prevent noise amplification [155]. To compute Eq. 3.16, FedGIMP estimates synthetic k-space data by projecting the synthetic image $S_{\theta_S}(w, n)$ through the imaging operator $A_{test}^{k,s} = \Omega^{k,s} \mathcal{F} B^{k,s}$, which embodies multiplication with coil sensitivities ($B^{k,s}$), Fourier transformation ($\mathcal{F}$), and undersampling with the prescribed sampling pattern ($\Omega^{k,s}$) [90]. Anatomical correspondence between synthetic and actual data is then achieved by minimizing $L_{DC}^{k,s}$. For each cross-section, the optimization is performed over θ_S, θ_M, z and n. Given the trained global generator $G_{\theta_G^*}$, synthesizer and mapper parameters are initialized as $\theta_S^1 \leftarrow \theta_S^*$ and

$\theta_M^1 \leftarrow \theta_M^*$, whereas instance-specific variables are randomly initialized as $z^1 \leftarrow z$ and $n^1 \leftarrow n$. Following a total of E iterations, the adapted prior is used to compute the final reconstruction:

$$\hat{m}_{k,s} = S_{\theta_S^E}(M_{\theta_M^E}(z^E \oplus v), n^E) \tag{3.17}$$

Thus, the synthetic image produced by the generator at the end of the optimization yields the final reconstructed image. Note that the values of z^E and n^E are not random but optimized.

Chapter 4

Methods

4.1 Architectural Details

The unconditional adversarial model in FedGIMP used a mapper with 8 FC layers receiving a standard normal vector and a one-hot binary encoding vector of site index as inputs, while outputting 32 intermediate latent variables. A synthesizer with 8 layers was used, where each layer contained a bilinear upsampling block for 2-fold increase of feature map resolution, followed by two serial cascades of Conv, NI and AdaIN blocks. The first layer received a 4x4 map of learnable constant values, initialized with ones, as input. The learnable noise variable was randomly initialized from a standard normal distribution. A discriminator with 8 layers was used, each containing a bilinear downsampling block for 2-fold reduction in resolution, and a convolution block with 3x3 kernel size. Leaky ReLU activation functions were used. Two separate channels at the generator's output and the discriminator's input were used to represent real and imaginary parts of complex MR images. During training, images were zero-padded to match the resolution of the output layer if needed. During inference, synthesized images were centrally cropped based on the size of the acquisition matrix prior to calculation of data-consistency loss. The synthesizer and discriminator were trained non-progressively, with all layers intact.

4.2 Competing Methods

FedGIMP was demonstrated against a traditional reconstruction (LORAKS), non-federated models (GAN_{cond}/GIMP), and federated conditional models (FL-MRCM, FedGAN, LG-Fed, FedMRI). Hyperparameter selection was performed based on validation performance. For each method, a single set of learning rate, number of epochs (non-federated), number of communication rounds and epochs (federated), and loss term weights were selected that yielded near-optimal performance across tasks. All models were trained via the Adam optimizer. A learning rate of $2\text{x}10^{-3}$ and δ=10 was selected for unconditional models; a learning rate of $2\text{x}10^{-4}$ was selected for conditional models. Decay rate parameters for the optimizer were adopted from previous studies as β_1=0.0, β_2=0.99 for unconditional [152], and β_1=0.5, β_2=0.99 for conditional models [53]. Training lasted 100 epochs for non-federated models, L=100 rounds and I=1 epochs for federated models. During inference, unconditional models enforced anatomical consistency to a test subject by minimizing a data-consistency loss. No notable improvement was observed in conditional models subjected to inference optimization based on data-consistency loss, so they used a strict data-consistency projection following a forward pass. Strict data consistency was enforced on all reconstructions prior to reporting. To ensure adherent implementation of competing methods, we utilized libraries from the public repositories shared by the originally proposing authors. Accordingly, we implemented LORAKS in Matlab[1], conditional models in PyTorch[2,3,4]. Unconditional models were implemented in TensorFlow to adopt libraries from a style-generative architecture for natural image synthesis[5]. Models were executed on a system with four Nvidia RTX 3090s.

FedGIMP: The proposed model was trained to synthesize coil-combined MR images. The model output magnitude images for single-coil experiments, and complex images with real and imaginary components as separate channels for multi-coil experiments. Inference was performed via the Adam optimizer, with

[1]https://mr.usc.edu/download/LORAKS2
[2]https://github.com/icon-lab/ProvoGAN
[3]https://github.com/guopengf/FL-MRCM
[4]https://github.com/chunmeifeng/FedMRI
[5]https://github.com/NVlabs/stylegan

optimized parameters transferred across consecutive cross-sections in a volume to improve convergence [90]. A learning rate of 10^{-2}, η=10^{-4} and E=1200 iterations were selected via cross validation. Reconstruction performance improves for higher E, yet the benefits become marginal beyond a certain level. Thus, we exercised early stopping based on the L-curve criterion to maintain a favorable compromise between performance and inference time [90].

LORAKS: A traditional autocalibrated low-rank reconstruction was performed [156]. The k-space neighborhood radius and the rank of LORAKS matrix were selected as (2,6) for single-coil reconstruction and (2,30) for multi-coil reconstruction.

GAN_{cond}: A non-federated conditional model was trained to map zero-filled (ZF) reconstruction of undersampled acquisitions to reference images of fully-sampled acquisitions [53]. Weights of (pixel-wise, adversarial, perceptual) losses were set as (100, 1, 100). Centralized training was performed following dataset aggregation across sites, albeit an unshared discriminator was used to process data coming from different sites as in FedGIMP. GAN_{cond} serves as a privacy-violating benchmark for conditional reconstruction.

GIMP: A non-federated unconditional model was trained based on the architecture and loss functions in FedGIMP. Centralized training was performed, other training and inference procedures were identical to FedGIMP. GIMP serves as a privacy-violating benchmark for unconditional reconstruction.

FL-MRCM: A federated conditional model was trained with adversarial alignment of latent representations across sites [70]. For fair comparison among FL methods, architecture and loss functions were adopted from GAN_{cond}. Latent representations from the residual backbone were passed through a convolution layer and provided to a domain-alignment network. Weights of (pixel-wise, adversarial, perceptual, reconstruction, domain-alignment) losses were set as (100, 1, 100, 0.5, 0.5).

FedGAN: A federated conditional model was trained with a shared encoder and

decoder across sites [157]. The architecture and loss functions followed GAN_{cond}. Weights of (pixel-wise, adversarial, perceptual) losses were set as (100, 1, 100).

LG-Fed: A federated conditional model was trained with site-specific encoders and a shared decoder [158]. The architecture and losses followed GAN_{cond}. Weights of (pixel-wise, adversarial, perceptual) losses were set as (100, 1, 100).

FedMRI: A federated conditional model was trained with a shared encoder and site-specific decoders [71]. The architecture and losses followed GAN_{cond}, albeit an added contrastive loss was included [71]. Weights of (pixel-wise, adversarial, perceptual, contrastive) losses were set as (100, 1, 100, 10).

4.3 Experiments

4.3.1 Datasets

FL experiments were conducted using an in-house dataset acquired at Bilkent University along with three public datasets (IXI http://brain-development.org/ixi-dataset/), fastMRI [68], BRATS [159]). We describe the in-house imaging protocol below (see related references for public datasets). Acquisitions were retrospectively undersampled using variable- (VD) and uniform-density (UD) patterns at acceleration rates R= (3x, 6x) [1]. There was no subject overlap between training, validation, and test sets. Each FL site corresponded to a distinct dataset, and all examined FL setups had 3 sites. The training set in each site aggregated MR images across multiple different contrasts. Training samples were randomly drawn from this aggregated set, without any special procedures for handling different contrasts. While modeling each contrast separately could enhance performance, we reasoned that training on mixed contrasts is a more realistic scenario given the ubiquity of multi-contrast protocols in clinical practice [69].

In-House: T_1-, T_2- and PD-weighted scans were performed in 10 subjects on a 3T Siemens Tim Trio scanner located at Bilkent University using a 32-channel

coil. An MP-RAGE sequence was used for T_1-weighted scans with TE/TI/TR = 3.87/1100/2000 ms, 20^o flip angle; and an FSE sequence was used for T_2-/PD-weighted scans with TE_{PD}/TE_{T2}/TR = 12/118/1000 ms, 90^o flip angle. All scans were performed with 192x256x176 mm^3 field-of-view and 1x1x2 mm^3 voxel size. Ethics approval was obtained from the local ethics committee, and all participants gave written-informed consent.

4.3.2 Single-Coil Reconstruction

Experiments were performed on IXI, fastMRI, and BRATS. Coil-combined magnitude images in each dataset were treated as single-coil data, so their analyses omitted the channel dimension of coil arrays. T_1-, T_2-, PD-weighted acquisitions in IXI and BRATS, T_1c-, T_2-, FLAIR-weighted acquisitions in fastMRI were considered. For each dataset, multi-contrast acquisitions of (40,5,10) subjects were reserved as (training, validation, test) sets, with 21 cross-sections per contrast randomly selected in each subject. As such, the training, validation and test sets within each dataset (i.e., each site) contained (840,105,210) cross-sections.

4.3.3 Multi-Coil Reconstruction

Experiments were performed on fastMRI brain, fastMRI knee, and In-House brain datasets, which all contained multi-coil k-space data. For fastMRI brain, T_1-, T_2-, FLAIR-weighted acquisitions from (36,6,9) subjects were reserved, with 8 cross-sections per contrast randomly selected in each subject. For fastMRI knee, PD-, PDFS-weighted acquisitions from (48,8,12) subjects were reserved, with 9 cross-sections per contrast. For In-House, T_1-, T_2-, PD-weighted acquisitions from (6,1,3) subjects were reserved, with 48 cross-sections per contrast in the training and validation sets, and with 24 cross-sections per contrast in the test set. As such, the training, validation and test sets within each dataset contained (864,144,216) cross-sections. Coil compression was performed onto 5 virtual coils [160]. Conditional models mapped multi-coil, complex ZF reconstructions of

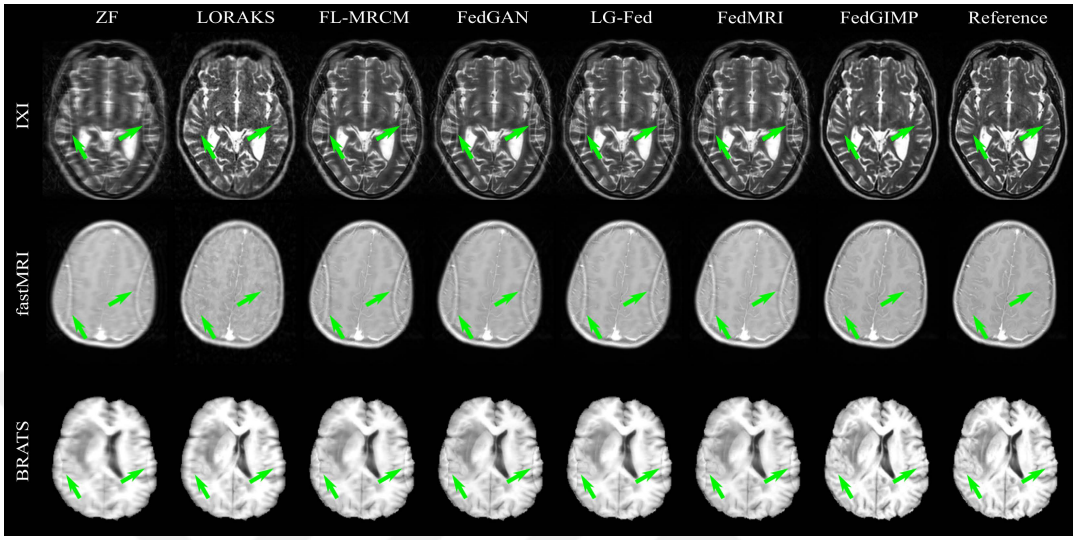

Figure 4.1: Representative reconstructions of a T_2-weighted acquisition in IXI, a T_1c-weighted acquisition in fastMRI, and a T_1-weighted acquisition in BRATS datasets at R=3x based on uniform-density patterns. Results are shown for ZF, LORAKS, FL-MRCM, FedGAN, LG-Fed, FedMRI, and FedGIMP along with the reference images. Conditional models were trained on variable-density patterns at R=3x.

undersampled data to reference images derived from fully-sampled data. GIMP and FedGIMP synthesized complex coil-combined MR images during training [154]. The imaging operator was only injected during inference to enforce data consistency based on multi-coil k-space data.

4.4 Quantitative Assessments

Reconstructed images were compared against Fourier reconstruction of fully-sampled acquisitions as reference. Peak signal-to-noise ratio (PSNR) and structural similarity index (SSIM) were measured, following normalization of images to [0 1]. Tables list mean and standard deviation of performance metrics across test subjects. Statistical significance of performance differences was assessed via Wilcoxon sign-rank tests.

Chapter 5

Results

5.1 Single-Coil Reconstruction

Domain shifts in the MR image distribution

Multi-site datasets of multi-contrast MRI data contain intrinsic domain shifts in the image distribution within and across sites [70]. To assess the influence of these intrinsic shifts, we examined performance when the imaging operator was matched across sites and across the training-test sets (Table 5.1). FedGIMP outperforms all competing methods ($p<0.05$), except on BRATS, R=6x where the privacy-violating benchmark GIMP performs similarly. On average across sites and R, FedGIMP yields 3.7dB PSNR, 3.0% SSIM improvement over the second-best FL method, demonstrating the efficacy of FedGIMP against heterogeneity in the MR image distribution.

Table 5.1: Single-coil reconstruction performance with the imaging operator matched across sites, and across the training-test sets. Boldface indicates the top-performing FL method.

			IXI		fastMRI		BRATS	
			PSNR ↑	SSIM↑	PSNR ↑	SSIM↑	PSNR ↑	SSIM↑
Non-fed	LORAKS	3x	28.6±2.5	69.9±6.5	29.1±4.6	70.4±11.3	35.1±4.0	95.1±0.5
		6x	26.0±1.9	61.9±6.6	26.0±3.9	62.0±12.2	31.7±3.6	92.3±0.9
	GAN_{cond}	3x	38.6±1.2	94.6±1.0	39.2±2.3	95.1±1.3	44.1±1.3	98.5±0.3
		6x	35.1±1.1	91.2±1.5	35.8±2.2	91.9±2.0	40.3±1.3	97.1±0.5
	GIMP	3x	42.2±1.4	98.2±0.5	40.6±2.2	97.1±1.0	50.6±1.9	99.7±0.1
		6x	37.6±1.3	96.4±1.0	36.6±2.3	94.5±1.6	45.4±1.7	99.2±0.2
Fed	FL-MRCM	3x	38.1±1.2	94.2±1.1	38.8±2.3	94.6±1.4	43.4±1.3	98.3±0.3
		6x	34.7±1.2	90.8±1.6	35.3±2.3	90.9±2.2	39.6±1.3	96.8±0.6
	FedGAN	3x	38.5±1.2	94.5±1.0	38.9±2.3	94.9±1.4	44.1±1.2	98.4±0.3
		6x	35.0±1.1	91.2±1.5	35.6±2.2	91.7±2.0	40.1±1.3	97.0±0.6
	LG-Fed	3x	38.4±1.2	94.3±1.0	38.9±2.3	94.9±1.4	44.0±1.3	98.4±0.3
		6x	34.8±1.0	90.6±1.4	35.6±2.3	91.6±2.0	40.1±1.3	97.1±0.6
	FedMRI	3x	38.6±1.2	94.4±1.0	39.0±2.3	94.9±1.3	44.2±1.3	98.5±0.3
		6x	34.9±1.1	90.5±1.5	35.5±2.2	91.4±2.0	40.3±1.4	97.2±0.5
	FedGIMP	3x	**42.9±1.5**	**98.5±0.5**	**41.1±2.2**	**97.4±0.8**	**50.9±1.9**	**99.7±0.1**
		6x	**37.8±1.4**	**96.5±1.0**	**36.9±2.2**	**94.8±1.4**	**45.4±1.7**	**99.2±0.2**

Domain shifts in the imaging operator

We then examined reconstruction performance under additional domain shifts due to the imaging operator. First, we considered homogeneous imaging operators across sites, while either acceleration rates (e.g., training at 3x, testing at 6x) or sampling densities (training with VD, testing with UD patterns) were mismatched across the training and test tests (Table 5.2). FedGIMP is the top performer among all methods ($p<0.05$), except for GIMP that performs similarly. Compared to the second-best FL method, FedGIMP offers 4.8dB PSNR, 4.0% SSIM improvement under mismatched R, and 4.5dB PSNR, 4.8% SSIM improvement under mismatched sampling density. Representative reconstructions under mismatched sampling density are shown in Fig. 4.1. Federated conditional models and LORAKS yield prominent aliasing artifacts and blurring, whereas FedGIMP achieves high visual acuity and improved artifact suppression due to its enhanced generalization performance.

Next, we considered heterogeneous imaging operators across sites for improved

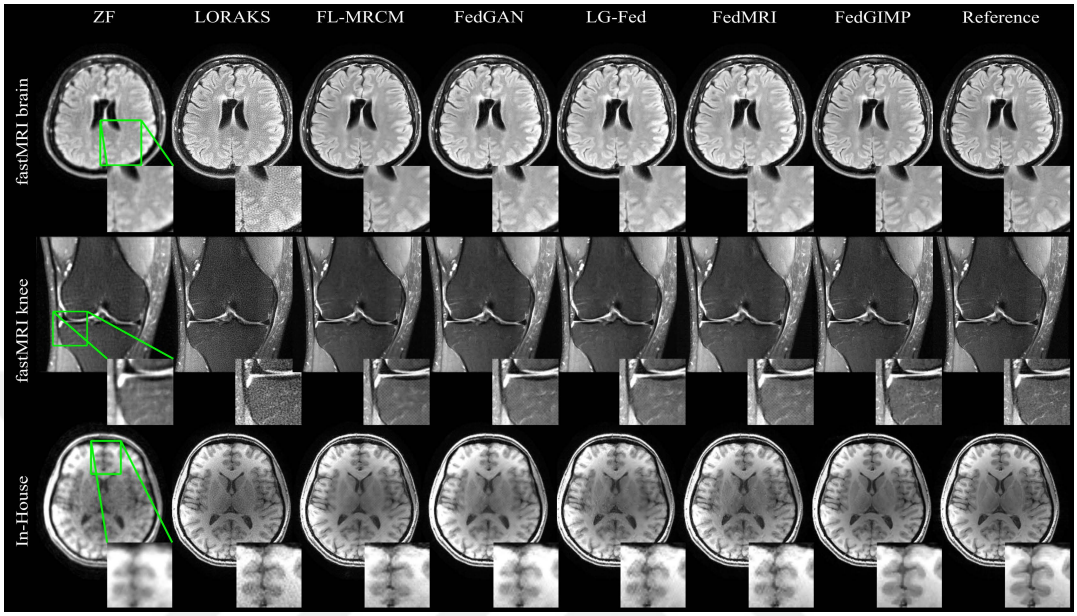

Figure 5.1: Representative reconstructions of a FLAIR acquisition of the brain in fastMRI, a fat suppressed PD-weighted acquisition of the knee in fastMRI, and a T_1-weighted acquisition of the brain in In-House datasets at R=6x. Results are shown for ZF, LORAKS, FL-MRCM, FedGAN, LG-Fed, FedMRI and FedGIMP along with the reference images. Conditional models were trained at R=3x.

flexibility in collaborations. We separately examined performance when the heterogeneous operators were matched or mismatched between the training-test sets (Table 5.3). When the training-test operators match, FedGIMP achieves the highest performance among competing methods ($p<0.05$), except for GIMP that performs similarly, and in BRATS where LG-Fed performs slightly better and GAN_{cond}, FedGAN, FedMRI perform similarly. When the training-test operators mismatch, FedGIMP achieves the highest performance among competing methods ($p<0.05$), except GIMP that performs similarly. Compared to the second-best FL method, FedGIMP offers 1.3dB PSNR and 2.7% SSIM improvement under matched operators, and 5.1dB PSNR, 3.0% SSIM improvement under mismatched operators.

5.2 Multi-Coil Reconstruction

Domain shifts in the MR image distribution

We first evaluated reconstruction performance when the imaging operator was matched across sites and training-test sets to assess intrinsic domain shifts due to the image distribution. Differing from single-coil experiments, multi-coil FL experiments were conducted on datasets containing two separate anatomies, i.e. the knee and the brain (Table 5.4). FedGIMP outperforms all competing methods ($p<0.05$), except GIMP that performs similarly. On average, FedGIMP achieves 6.3dB PSNR, 4.2% SSIM improvement over the second-best FL method. These results corroborate the efficacy of FedGIMP in multi-coil settings, and its efficiency in coping with heterogeneity in the image distribution due to diverse anatomy.

Domain shifts in the imaging operator

We also evaluated reconstruction performance under additional domain shifts due to mismatched imaging operators with different acceleration rates across the training-test sets (Table 5.5). FedGIMP is the top performer among competing methods ($p<0.05$), except for GIMP that performs similarly. FedGIMP offers 6.9dB PSNR, 4.5% SSIM improvement over the second-best FL method. Representative reconstructions are shown in Fig. 5.1. LORAKS suffers from noise amplification, and conditional models yield notable blur and artifacts. In contrast, FedGIMP achieves high visual acuity while mitigating noise amplification.

5.3 Heterogeneity of MRI Data

FL of a multi-site model on homogeneous datasets would correspond to training on more samples from a common distribution, and model performance would

solely reflect the influence of prolonged training. To rule out this nuisance explanation, we first measured the intra-site and inter-site heterogeneity of cross-sectional images in the training set. For intra-site heterogeneity, the image distributions were compared among individual subjects within a given site. For inter-site heterogeneity, the image distributions were compared among individual subjects from separate sites. Frechet inception distance (FID) was used to measure dissimilarity of distributions. As shown in Fig. 5.2, we find varying albeit notable levels of heterogeneity in each site. Importantly, inter-site heterogeneity is significantly higher than intra-site heterogeneity for all sites ($p<0.05$). The increase from intra-site to inter-site FID score is 9.2 for single-coil (a 94.1% increase) and 5.0 for multi-coil (a 105.0% increase) settings. We then examined the influence of this apparent heterogeneity on single-site models trained on local data from individual sites. Specifically, we assessed the loss incurred in single-site models due to domain shifts in the image distribution between training and test sites. To do this, we measured the within-site and across-site reconstruction performances of GAN_{cond} and GIMP while the imaging operator was matched across sites and training-test sets. We find that across-site performance is lower than within-site performance for both models ($p<0.05$). On average, GAN_{cond} suffers from 1.9dB PSNR, 2.0% SSIM loss in single-coil, and 2.5dB PSNR, 1.8% SSIM loss in multi-coil reconstruction. In contrast, GIMP shows relatively lower 1.5dB PSNR, 0.6% SSIM loss in single-coil, and 0.8dB PSNR, 0.2% SSIM loss in multi-coil reconstruction. Taken together, these findings indicate that our results cannot be attributed to a lack of data heterogeneity across sites. Furthermore, the adaptive GIMP model shows higher reliability against data heterogeneity compared to the non-adaptive GAN_{cond} model.

5.4 Ablation Studies

Several lines of ablation studies were conducted to demonstrate the individual design elements in FedGIMP. To assess the contribution of using an adaptive prior, we built a static-prior variant that optimized model inputs but kept model weights fixed as in [89]. To assess the federated training of the prior, we built

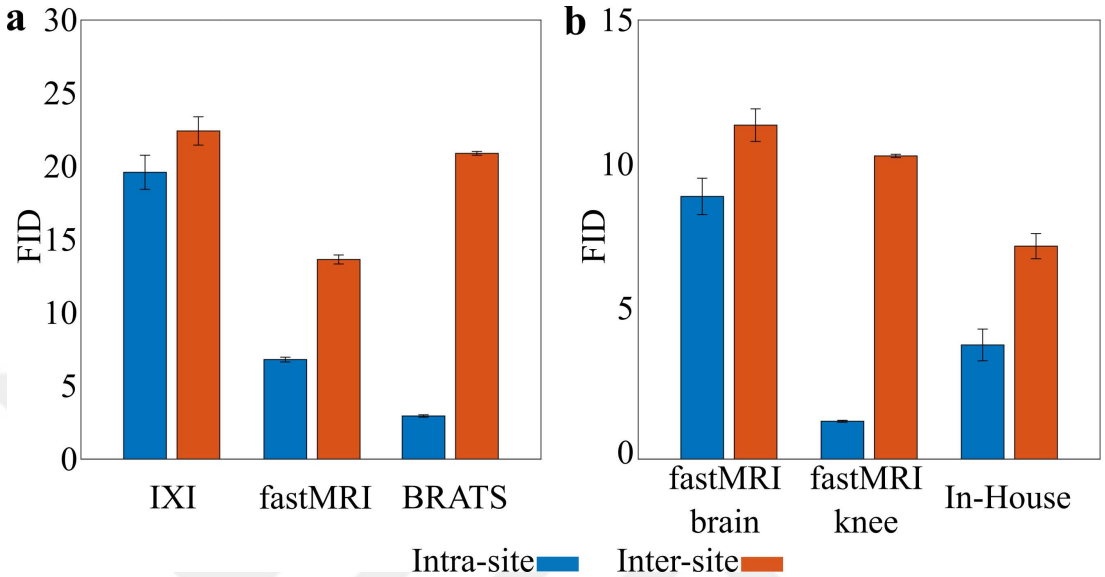

Figure 5.2: Heterogeneity of MRI datasets were examined by measuring FID between respective image distributions, reported as mean±se (error bars) across subjects. Intra-site (blue) and inter-site (orange) heterogeneity is shown for each dataset examined for (a) single-coil, (b) multi-coil reconstruction.

an untrained variant where inference adaptation was performed on a randomly initialized generator. To assess the mapper, we built a mapper-ablated variant that only used a synthesizer as in [67]. To assess the site index, we built a site-index-ablated variant that used a mapper producing site-general latent variables. To assess the mapper adaptation to indirectly optimize latents, we built a static-mapper variant that directly optimized latents as in [90]. Table 5.6 demonstrates that FedGIMP outperforms all ablated variants consistently across sites. These results indicate the importance of prior adaptation, learning of a high-quality prior, inclusion of the mapper, inclusion of the site index, and indirect optimization of latents for improving MRI reconstruction performance. In particular, utilizing a site-index in the mapper achieves 1.1dB PSNR and 0.5% SSIM improvement, and in theory the benefits of the site index should increase further for growing number of sites and data heterogeneity.

Next, we evaluated the influence of the site index on practicality when a site joins or leaves training abruptly. Note that an additional site can join training by designating spare digits in the site-index vector, and an existing site can easily abstain from training given that its digit in the site-index vector is not

reassigned to a different site. Thus, we examined FedGIMP's performance under scenarios where an initially held-out site joined the training halfway, and where an initially included site left the training halfway. In both scenarios, FedGIMP was compared against the site-index-ablated variant, and against the original model trained with all sites intact. Performance metrics are listed in Table 5.7. FedGIMP with joining or abstaining sites outperforms the ablated variant by 1.2dB PSNR, 0.6% SSIM on average; and it offers similar performance to the original FedGIMP trained with all sites intact. These results suggest that the site index does not limit practicality of model training, and it rather introduces a degree of reliability against joining or abstaining sites.

Lastly, we examined the utility of local discriminators in FedGIMP. A primary benefit of unshared discriminators is theoretical improvements in privacy against inference attacks [161]. Local discriminators also reduce communication load by 46.7% for FedGIMP, given that the discriminator and generator have comparable complexity (23.0 versus 26.3 million parameters). Beyond these theoretical benefits, we assessed the influence of local discriminators on model performance. First, we inspected the training losses for the generator (unreported). The loss curves showed smooth behavior across training epochs, with no apparent signs of mode collapse [152]. Second, we compared FedGIMP against a variant with shared discriminators across sites. Metrics in Table 5.7 indicate on par performance with both models. These results suggest that there are no apparent performance drawbacks to using local discriminators.

5.5 Inference Times

Inference times of competing methods are listed in Table 5.8. Matching architectures yield near identical inference time, so results are reported for LORAKS, non-adaptive models (GAN_{cond}, FL-MRCM, FedGAN, LG-Fed, FedMRI), and adaptive models (GIMP, FedGIMP). Inference time for adaptive models is high

compared to non-adaptive models that use a single forward pass, and it is relatively more proximate to LORAKS. Yet, this computational load enables substantial benefits in reconstruction performance. For instance, FedGIMP achieves 10.4dB PSNR, 14.7% SSIM improvement over LORAKS, and 6.0dB PSNR, 3.1% SSIM improvement over the top-contending non-adaptive model across single- and multi-reconstruction tasks at R=3x with matched imaging operators across sites and training/test sets. Furthermore, FedGIMP enhances tissue depiction visually with lower artifacts and higher acuity than competing methods. Note also that FedGIMP's performance increases across inference iterations, so the number of iterations can be adjusted to maximize performance per available compute time in specific applications. Thus, FedGIMP offers a flexible trade-off between reconstruction quality and compute time, which might facilitate practical use.

Table 5.2: Single-coil reconstruction performance with the imaging operator mismatched across the training-test sets, $A \rightarrow B$ denotes the domain shift in R (upper panel) / sampling densities (lower panel).

Acceleration Rate (6x→3x or 3x→6x)								
			IXI		fastMRI		BRATS	
			PSNR ↑	SSIM↑	PSNR ↑	SSIM↑	PSNR ↑	SSIM↑
Non-fed	LORAKS	3x	28.6±2.5	69.9±6.5	29.1±4.6	70.4±11.3	35.1±4.0	95.1±0.5
		6x	26.0±1.9	61.9±6.6	26.0±3.9	62.0±12.2	31.7±3.6	92.3±0.9
	GAN_{cond}	3x	37.8±1.1	92.9±1.1	38.0±1.9	93.7±1.4	42.2±1.3	97.8±0.4
		6x	33.5±1.2	89.6±1.7	34.3±2.4	90.2±2.4	39.3±1.4	96.9±0.6
	GIMP	3x	42.2±1.4	98.2±0.5	40.6±2.2	97.1±1.0	50.6±1.9	99.7±0.1
		6x	37.6±1.3	96.4±1.0	36.6±2.3	94.5±1.6	45.4±1.7	99.2±0.2
Fed	FL-MRCM	3x	37.4±1.1	92.6±1.2	37.3±2.0	92.8±1.7	40.7±1.4	96.9±0.7
		6x	33.1±1.3	88.5±2.1	33.9±2.4	89.1±2.6	38.6±1.3	96.4±0.7
	FedGAN	3x	37.5±1.1	92.7±1.2	38.1±1.9	93.8±1.4	41.9±1.2	97.6±0.5
		6x	33.3±1.2	89.2±1.7	34.1±2.4	89.8±2.5	39.1±1.3	96.8±0.6
	LG-Fed	3x	37.6±1.0	92.9±1.0	37.8±1.9	93.4±1.6	42.2±1.3	97.8±0.5
		6x	33.9±1.2	89.9±1.5	34.3±2.3	90.2±2.3	39.6±1.3	97.0±0.6
	FedMRI	3x	37.6±1.0	92.8±1.1	37.8±1.8	93.5±1.5	42.7±1.3	98.0±0.4
		6x	34.1±1.2	90.2±1.5	34.3±2.4	89.9±2.4	39.6±1.4	97.1±0.6
	FedGIMP	3x	**42.9±1.5**	**98.5±0.5**	**41.1±2.2**	**97.4±0.8**	**50.9±1.9**	**99.7±0.1**
		6x	**37.8±1.4**	**96.5±1.0**	**36.9±2.2**	**94.8±1.4**	**45.4±1.7**	**99.2±0.2**
Sampling Density (VD→UD)								
			IXI		fastMRI		BRATS	
			PSNR ↑	SSIM↑	PSNR ↑	SSIM↑	PSNR ↑	SSIM↑
Non-fed	LORAKS	3x	25.5±1.4	80.9±3.7	26.1±2.9	79.9±6.5	31.5±2.9	94.5±0.6
		6x	21.7±0.8	67.4±4.5	21.2±1.7	63.9±7.1	24.7±2.4	85.6±1.4
	GAN_{cond}	3x	30.3±1.0	89.5±1.5	31.0±2.8	88.7±3.2	37.0±1.4	96.1±0.7
		6x	24.2±0.7	77.0±2.9	25.1±1.9	76.5±4.5	30.4±1.3	90.0±1.3
	GIMP	3x	35.3±1.6	95.7±1.1	35.1±2.3	93.8±1.6	47.0±2.1	99.5±0.2
		6x	26.8±0.9	84.0±2.4	28.1±2.6	82.3±3.9	33.4±1.4	93.6±1.0
Fed	FL-MRCM	3x	30.5±1.0	89.8±1.3	30.7±2.6	87.5±3.1	36.1±1.5	95.1±0.9
		6x	23.9±0.6	74.8±2.5	24.5±1.6	73.4±3.9	29.4±1.3	86.8±1.7
	FedGAN	3x	30.2±1.0	89.3±1.5	31.0±2.7	89.0±3.1	37.1±1.4	96.2±0.7
		6x	24.1±0.7	76.6±3.0	25.0±1.9	76.4±4.6	30.2±1.3	89.8±1.3
	LG-Fed	3x	30.6±1.1	90.0±1.4	31.0±2.7	88.7±3.1	36.9±1.5	96.1±0.8
		6x	24.2±0.7	77.4±2.9	25.1±1.9	76.5±4.7	30.2±1.3	89.9±1.4
	FedMRI	3x	30.7±1.1	90.4±1.3	31.1±2.7	89.0±2.9	37.2±1.5	96.3±0.7
		6x	24.3±0.7	77.8±2.6	25.0±1.8	76.1±4.4	30.4±1.3	90.3±1.3
	FedGIMP	3x	**35.1±1.4**	**95.4±1.0**	**35.3±2.4**	**94.2±1.7**	**47.4±2.2**	**99.6±0.2**
		6x	**26.6±1.0**	**83.9±2.5**	**28.0±2.5**	**82.3±4.0**	**33.4±1.4**	**93.4±1.0**

Table 5.3: Single-coil reconstruction performance with heterogeneous imaging operators across sites. The operators were either matched (upper panel) or mismatched (lower panel) across the training-test sets.

Matched across training-test sets							
		IXI (9x, VD)		fastMRI (3x, VD)		BRATS (6x, UD)	
		PSNR ↑	SSIM↑	PSNR ↑	SSIM↑	PSNR ↑	SSIM↑
Non-fed	LORAKS	25.0±1.6	58.8±6.5	29.1±4.6	70.4±11.3	24.7±2.4	85.6±1.4
	GAN_{cond}	33.4±1.1	88.8±1.7	39.0±2.2	94.9±1.3	33.0±1.2	93.2±1.0
	GIMP	35.5±1.3	95.0±1.3	40.6±2.2	97.1±1.0	33.4±1.4	93.6±1.0
Fed	FL-MRCM	32.9±1.0	88.5±1.5	37.6±2.3	93.1±1.7	30.5±1.3	89.9±1.4
	FedGAN	33.0±1.0	88.4±1.5	38.0±1.9	93.5±1.5	32.5±1.2	92.9±0.9
	LG-Fed	33.4±1.0	88.8±1.6	38.9±2.3	94.9±1.4	**33.9±1.3**	**94.2±0.9**
	FedMRI	33.4±1.0	88.7±1.5	38.9±2.2	94.8±1.3	33.0±1.2	93.2±1.0
	FedGIMP	**35.6±1.4**	**95.2±1.4**	**41.1±2.2**	**97.4±0.8**	33.4±1.4	93.4±1.0
Mismatched across training-test sets							
		IXI (9x, VD)→(3x, UD)		fastMRI (3x, VD)→(6x, UD)		BRATS (6x, UD)→(3x, VD)	
		PSNR ↑	SSIM↑	PSNR ↑	SSIM↑	PSNR ↑	SSIM↑
Non-fed	LORAKS	25.5±1.4	80.9±3.7	21.2±1.7	63.9±7.1	35.1±4.0	95.1±0.5
	GAN_{cond}	31.3±1.1	91.2±1.3	26.1±2.3	79.4±4.8	42.1±1.0	97.7±0.3
	GIMP	35.3±1.6	95.7±1.1	28.1±2.6	82.3±3.9	50.6±1.9	99.7±0.1
Fed	FL-MRCM	31.9±0.9	91.6±1.1	25.8±2.0	77.7±4.3	40.8±1.2	97.0±0.6
	FedGAN	32.3±1.0	92.5±1.1	25.9±2.1	79.3±4.5	40.6±1.3	96.7±0.7
	LG-Fed	31.5±1.0	91.1±1.2	24.9±1.9	75.8±4.8	38.0±1.0	94.6±0.8
	FedMRI	31.7±1.1	91.4±1.2	24.9±1.8	75.8±4.5	37.8±1.1	94.2±1.0
	FedGIMP	**35.1±1.4**	**95.4±1.0**	**28.0±2.5**	**82.3±4.0**	**50.9±1.9**	**99.7±0.1**

Table 5.4: Multi-coil reconstruction performance with the imaging operator matched across sites, and the training-test sets.

			fastMRI brain		fastMRI knee		In-House brain	
			PSNR ↑	SSIM↑	PSNR ↑	SSIM↑	PSNR ↑	SSIM↑
Non-fed	LORAKS	3x	36.1±0.9	89.6±1.1	33.0±1.4	79.0±2.3	51.1±1.0	99.3±0.1
		6x	30.8±1.6	80.3±2.6	30.9±1.5	74.1±2.7	39.3±1.4	95.7±0.9
	GAN_{cond}	3x	40.1±0.9	95.6±0.6	36.1±1.2	89.9±1.6	43.5±1.0	98.7±0.2
		6x	36.3±0.9	91.9±0.9	33.2±1.1	83.1±2.4	38.8±0.9	96.9±0.5
	GIMP	3x	47.5±0.9	98.8±0.2	43.6±1.2	97.5±0.4	52.4±1.1	99.6±0.1
		6x	40.8±0.9	95.7±0.5	38.0±1.3	91.6±1.3	43.9±1.0	98.5±0.2
Fed	FL-MRCM	3x	39.4±0.9	95.8±0.5	36.9±1.3	90.6±1.3	40.4±0.9	97.5±0.4
		6x	35.9±0.8	92.2±0.8	33.8±1.2	82.1±2.4	36.0±0.8	95.0±0.7
	FedGAN	3x	39.8±0.9	95.6±0.5	37.0±1.2	90.0±1.5	41.7±1.1	98.1±0.3
		6x	35.9±0.8	92.1±0.9	34.0±1.2	82.7±2.5	36.7±0.9	95.7±0.7
	LG-Fed	3x	39.8±0.8	95.7±0.5	36.6±1.2	89.5±1.6	42.8±0.9	98.5±0.2
		6x	35.9±0.8	92.4±0.8	33.7±1.2	82.2±2.5	38.4±0.9	96.6±0.5
	FedMRI	3x	39.9±0.9	95.8±0.5	36.8±1.2	89.7±1.6	43.0±0.9	98.6±0.2
		6x	36.1±0.9	92.4±0.8	33.7±1.2	81.7±2.6	38.0±0.9	96.6±0.5
	FedGIMP	3x	**47.2±0.9**	**98.7±0.2**	**43.3±1.2**	**97.4±0.4**	**52.8±1.2**	**99.6±0.1**
		6x	**40.7±0.9**	**95.7±0.5**	**37.9±1.3**	**91.5±1.4**	**44.0±1.0**	**98.5±0.2**

Table 5.5: Multi-coil reconstruction performance with the imaging operator mismatched across training-test sets.

			fastMRI brain		fastMRI knee		In-House brain	
			PSNR ↑	SSIM↑	PSNR ↑	SSIM↑	PSNR ↑	SSIM↑
Non-Fed	LORAKS	3x	36.1±0.9	89.6±1.1	33.0±1.4	79.0±2.3	51.1±1.0	99.3±0.1
		6x	30.8±1.6	80.3±2.6	30.9±1.5	74.1±2.7	39.3±1.4	95.7±0.9
	GAN_{cond}	3x	39.0±0.8	95.1±0.5	35.8±1.1	89.5±1.5	41.5±0.9	98.4±0.2
		6x	36.4±1.0	92.2±1.0	33.4±1.2	83.3±2.4	37.4±1.0	95.8±0.6
	GIMP	3x	47.5±0.9	98.8±0.2	43.6±1.2	97.5±0.4	52.2±1.1	99.7±0.1
		6x	40.8±0.9	95.7±0.5	38.0±1.3	91.6±1.3	43.6±1.0	98.4±0.2
Fed	FL-MRCM	3x	37.7±0.8	94.8±0.8	35.8±1.2	88.5±2.3	37.9±0.8	96.0±0.7
		6x	36.3±1.0	93.0±0.7	34.2±1.3	83.9±1.7	35.9±0.9	94.7±0.6
	FedGAN	3x	38.4±0.8	95.0±0.5	36.1±1.2	88.7±1.7	39.7±0.9	97.7±0.4
		6x	36.0±1.1	92.6±0.9	34.2±1.2	84.0±2.3	36.2±1.1	95.3±0.7
	LG-Fed	3x	38.6±0.7	95.1±0.5	35.8±1.2	88.2±1.7	41.3±0.8	98.1±0.3
		6x	36.2±1.0	92.8±0.9	34.0±1.2	83.5±2.4	37.4±1.1	96.1±0.6
	FedMRI	3x	38.9±0.8	95.1±0.5	35.9±1.2	88.0±1.8	40.8±0.8	98.2±0.3
		6x	36.2±1.0	92.8±0.9	34.1±1.2	83.3±2.4	37.6±1.0	95.9±0.6
	FedGIMP	3x	**47.2±0.9**	**98.7±0.2**	**43.3±1.2**	**97.4±0.4**	**52.8±1.2**	**99.6±0.1**
		6x	**40.7±0.9**	**95.7±0.5**	**37.9±1.3**	**91.5±1.4**	**44.0±1.0**	**98.5±0.2**

Table 5.6: Reconstruction performance of FedGIMP and ablated variants at R=3x, with matched imaging operators across sites.

	IXI		fastMRI		BRATS	
	PSNR ↑	SSIM↑	PSNR ↑	SSIM↑	PSNR ↑	SSIM↑
Static Prior	29.5±0.7	71.5±2.4	30.5±1.9	74.9±4.8	34.5±1.2	88.0±1.9
Untrained	34.7±1.0	88.6±1.9	35.4±2.0	90.3±2.4	38.7±1.4	95.4±1.1
No Mapper	40.1±1.2	97.0±0.7	38.8±2.0	95.7±1.2	47.2±1.8	99.2±0.3
No Site-Index	41.0±1.3	97.7±0.7	40.2±2.1	96.8±1.0	50.5±1.9	99.6±0.2
Static Mapper	42.3±1.4	98.2±0.5	40.7±2.2	97.1±0.9	50.6±1.9	99.6±0.1
FedGIMP	**42.9±1.5**	**98.5±0.5**	**41.1±2.2**	**97.4±0.8**	**50.9±1.9**	**99.7±0.1**

Table 5.7: Reconstruction performance at R=3x with matched imaging operators. Results listed for FedGIMP with all sites, a joining site (FedGIMP-join), and an abstaining site (FedGIMP-abs); for the site-index-ablated variant with a joining site (NSI-join) and an abstaining site (NSI-abs); and for a variant with shared discriminators. The joining and abstaining sites were taken as BRATS.

	IXI		fastMRI		BRATS	
	PSNR ↑	SSIM↑	PSNR ↑	SSIM↑	PSNR ↑	SSIM↑
FedGIMP	42.9±1.5	98.5±0.5	41.1±2.2	97.4±0.8	50.9±1.9	99.7±0.1
FedGIMP-join	42.7±1.4	98.4±0.5	41.0±2.2	97.3±0.9	50.6±1.9	99.7±0.1
FedGIMP-abs	43.0±1.6	98.5±0.5	41.0±2.3	97.3±0.9	50.9±2.0	99.7±0.1
NSI-join	40.9±1.2	97.5±0.6	39.9±2.2	96.6±1.1	49.8±1.9	99.6±0.2
NSI-abs	40.4±1.2	97.2±0.7	40.1±2.1	96.8±1.0	50.7±1.9	99.7±0.1
Shared D	42.9±1.5	98.4±0.5	41.2±2.2	97.4±0.8	51.1±1.9	99.7±0.1

Table 5.8: Average inference time in secs per cross-section for single-coil and multi-coil reconstructions.

	LORAKS	Non-adaptive	Adaptive
Single-coil	2.40	0.034	20.30
Multi-coil	6.99	0.080	27.89

Chapter 6

Discussion

Multi-site imaging data collected under diverse protocols/devices can contain heterogeneity in the image distribution and the imaging operator across sites, as well as across the training-test sets [86]. Recent studies have proposed latent-space alignment or split-network approaches based on conditional reconstruction models to address across-site heterogeneity [70, 71]. Yet, conditional models are susceptible to domain shifts in the imaging operator pertained to undersampled data [90]. In contrast, FedGIMP decouples the undersampling characteristics from the prior to improve reliability against heterogeneity in the imaging operator. Experiments on multi-site datasets demonstrate that FedGIMP yields superior performance against federated conditional models under various imaging scenarios with varying acceleration rates, sampling density across sites, and across the training-test sets. Therefore, FedGIMP can improve flexibility in multi-site collaborations by permitting heterogeneous protocols.

A practical concern for MRI reconstruction is the computational cost of training and inference. Here, we primarily considered adversarial architectures for competing methods. Previous conditional methods additionally compute either a cross-site alignment loss on latent-space representations [70], or a weighted-contrastive loss across sites based on local encoder weights [71]. Furthermore, while conditional models are retrained for each configuration of acceleration rate

and sampling density, FedGIMP trains a single MRI prior to reconstruct with various different imaging operators. Thus, FedGIMP offers a simpler training procedure. During inference, conditional models offer fast processing in a single forward-pass, whereas FedGIMP uses an iterative prior adaptation that elevates computational burden. Still, FedGIMP's inference time is generally compatible with clinically-adopted implementations of traditional reconstruction methods, implying practical feasability [156, 162]. To improve efficiency in time-critical applications, prior adaptation across an MRI volume can be accelerated by parallel computation via distributing cross-sections across multiple GPUs.

GAN models are commonly trained to generate new image samples from low-dimensional random variables [152]. While the stochasticity of generated images may be undesirable for reconstruction, previous studies have employed GAN-based methods to recover MRI images without notable hallucinations [49,51,53,67,76,77]. To prevent artificial structures, these methods have incorporated data-consistency modules. Similarly in FedGIMP, the subject-specific prior adaptation based on data-consistency constrains the reconstruction by incorporating information regarding coil sensitivities, sampling patterns and measured k-space data from the actual subject. Under this control procedure, we have not encountered artificial structures based on our visual inspections, as also indicated by high performance metrics across various datasets. Multi-site data analyzed here for single- and multi-coil reconstructions generally contained a considerable number of subjects. While the In-House dataset had relatively fewer subjects, we analyzed it given the scarcity of public datasets providing multi-coil, multi-contrast MRI data. It remains important future work to systematically validate the proposed method and its anatomical fidelity on broader patient cohorts.

FL methods transfer model weights across sites instead of MRI data to lower privacy risks. Still, security concerns can arise from backdoor attacks where an adversary poisons training updates to corrupt models and elicits diagnostically-inaccurate reconstructions [57]. Previously proposed non-adaptive models freezing model weights following training can be more sensitive to model corruption. In contrast, FedGIMP adapts its MRI prior to each test sample, so it can potentially alleviate corruption during inference [155]. Learning-based models can also

be vulnerable to inference attacks on models aiming to leak sensitive information about training data [57]. Differential privacy between training and synthetic samples in adversarial models substantially improves for large and diverse training datasets as encountered in FL settings [163]. Furthermore, FedGIMP uses a shared generator without direct access to data and unshared discriminators that are not communicated [164]. Nonetheless, resilience against inference attacks can be improved by adopting differential-privacy procedures [165, 166]. Future studies are warranted to systematically characterize the privacy-preserving abilities of FedGIMP, including the benefits of local discriminators.

Here we aggregated local models using the relatively common and simple FedAvg algorithm, which has been successfully employed in many previous FL studies [64]. Model aggregation was performed via a weighted linear combination, where the weight for each site is taken as the ratio of the number of local training samples to the number of all training samples across sites. Performance improvements might be possible with data-driven combination based on model comparisons [167] or neural networks [168]. However, data-driven model combination typically involves storage and computation of additional models, and transfer of additional model updates. Future work is warranted to examine the comparative benefits of unlearned versus learned aggregation of local models in MRI reconstruction.

FedGIMP trains an MRI prior over the distribution of high-quality MR images, uninformed regarding the reconstruction task. Several lines of development can be considered for improved performance. First, multi-supervised networks concurrently operating in image and k-space domains have recently been introduced for MRI reconstruction [11, 50]. FedGIMP might also benefit from a hybrid of image and k-space MR priors. Second, self-supervised training of parallel networks based on contrastive learning has been proposed [81, 83]. Contrastive learning strategies might alleviate the need for fully-sampled acquisitions for training the MRI prior in FedGIMP. In principle, the federated prior can be adapted for other inverse problems such as MRI super-resolution or synthesis. A simple approach would be to train task-specific models using a synthetic dataset generated via

the MRI prior. Alternatively, the trained prior can serve as a non-adaptive plug-and-play regularizer in optimization problems [89]. To adapt the prior during inference, the imaging operator for the reconstruction task would have to be replaced with corresponding operators in target tasks.

Chapter 7

Conclusion

In this thesis, we introduced a novel MRI reconstruction based on federated learning of a generative MRI prior and inference adaptation via injection of subject-specific imaging operators onto this prior. Benefits over state-of-the-art federated and traditional methods were demonstrated in multi-site MRI datasets. Improved generalization against domain shifts renders FedGIMP a promising candidate for multi-site collaborations in accelerated MRI. FedGIMP might also be used for physics-based reconstruction in other modalities such as CT, PET, or ultrasound by modifying its imaging operator.

Bibliography

[1] M. Lustig, D. Donoho, and J. M. Pauly, "Sparse MRI: The application of compressed sensing for rapid MR imaging," *Magn Reson Med*, vol. 58, no. 6, pp. 1182–1195, 2007.

[2] B. Zhao, W. Lu, T. K. Hitchens, F. Lam, C. Ho, and Z.-P. Liang, "Accelerated mr parameter mapping with low-rank and sparsity constraints," *Magn Reson Med*, vol. 74, no. 2, pp. 489–498, 2015.

[3] S. Wang, Z. Su, L. Ying, X. Peng, S. Zhu, F. Liang, D. Feng, and D. Liang, "Accelerating magnetic resonance imaging via deep learning," in *Int Sym Biomed Imaging*, 2016, pp. 514–517.

[4] K. Hammernik, T. Klatzer, E. Kobler, M. P. Recht, D. K. Sodickson, T. Pock, and F. Knoll, "Learning a variational network for reconstruction of accelerated MRI data," *Magn Reson Med*, vol. 79, no. 6, pp. 3055–3071, 2017.

[5] K. Kwon, D. Kim, and H. Park, "A parallel MR imaging method using multilayer perceptron," *Med Phys*, vol. 44, no. 12, pp. 6209–6224, 2017.

[6] S. U. H. Dar, M. Özbey, A. B. Çatlı, and T. Çukur, "A transfer-learning approach for accelerated MRI using deep neural networks," *Magn Reson Med*, vol. 84, no. 2, pp. 663–685, 2020.

[7] Y. Han, J. Yoo, H. H. Kim, H. J. Shin, K. Sung, and J. C. Ye, "Deep learning with domain adaptation for accelerated projection-reconstruction MR," *Magn Reson Med*, vol. 80, pp. 1189–1205, 2018.

[8] Y. Yang, J. Sun, H. Li, and Z. Xu, "ADMM-CSNet: A deep learning approach for image compressive sensing," *IEEE Trans Pattern Anal Mach Intell*, vol. 42, no. 3, pp. 521–538, 2020.

[9] M. Akçakaya, S. Moeller, S. Weingärtner, and K. Uğurbil, "Scan-specific robust artificial-neural-networks for k-space interpolation (RAKI) reconstruction: Database-free deep learning for fast imaging," *Magn Reson Med*, vol. 81, no. 1, pp. 439–453, 2019.

[10] L. Xiang, Y. Chen, W. Chang, Y. Zhan, W. Lin, Q. Wang, and D. Shen, "Deep-learning-based multi-modal fusion for fast mr reconstruction," *IEEE Trans Biomed Eng*, vol. 66, no. 7, pp. 2105–2114, 2019.

[11] S. Wang, Z. Ke, H. Cheng, S. Jia, L. Ying, H. Zheng, and D. Liang, "DIMENSION: Dynamic MR imaging with both k-space and spatial prior knowledge obtained via multi-supervised network training," *NMR in Biomed*, vol. 35, no. 4, p. e4131, 2022.

[12] A. Güngör, S. U. Dar, Şaban Öztürk, Y. Korkmaz, H. A. Bedel, G. Elmas, M. Ozbey, and T. Çukur, "Adaptive diffusion priors for accelerated mri reconstruction," *Medical Image Analysis*, vol. 88, p. 102872, 2023.

[13] H. A. Bedel, I. Sivgin, O. Dalmaz, S. U. Dar, and T. Çukur, "Bolt: Fused window transformers for fmri time series analysis," *Medical Image Analysis*, vol. 88, p. 102841, 2023.

[14] Şaban Öztürk, E. Çelik, and T. Çukur, "Content-based medical image retrieval with opponent class adaptive margin loss," *Information Sciences*, vol. 637, p. 118938, 2023.

[15] E. Ilicak, E. U. Saritas, and T. Çukur, "Automated parameter selection for accelerated mri reconstruction via low-rank modeling of local k-space neighborhoods," *Zeitschrift für Medizinische Physik*, vol. 33, no. 2, pp. 203–219, 2023.

[16] F. T. Yarman Vural, S. D. Newman, T. Çukur, and I. Önal Ertugrul, "Editorial: Machine learning methods for human brain imaging," *Frontiers in Neuroinformatics*, vol. 17, 2023.

[17] M. Yurt, O. Dalmaz, S. Dar, M. Ozbey, B. Tınaz, K. Oguz, and T. Çukur, "Semi-supervised learning of mri synthesis without fully-sampled ground truths," *IEEE Transactions on Medical Imaging*, vol. 41, no. 12, pp. 3895–3906, 2022.

[18] A. Güngör, B. Askin, D. A. Soydan, E. U. Saritas, C. B. Top, and T. Çukur, "Transms: Transformers for super-resolution calibration in magnetic particle imaging," *IEEE Transactions on Medical Imaging*, vol. 41, no. 12, pp. 3562–3574, 2022.

[19] Öztürk and T. Çukur, "Deep clustering via center-oriented margin free-triplet loss for skin lesion detection in highly imbalanced datasets," *IEEE Journal of Biomedical and Health Informatics*, vol. 26, no. 9, pp. 4679–4690, 2022.

[20] O. Dalmaz, M. Yurt, and T. Çukur, "Resvit: Residual vision transformers for multimodal medical image synthesis," *IEEE Transactions on Medical Imaging*, vol. 41, no. 10, pp. 2598–2614, 2022.

[21] Y. Korkmaz, S. U. H. Dar, M. Yurt, M. Özbey, and T. Çukur, "Unsupervised mri reconstruction via zero-shot learned adversarial transformers," *IEEE Transactions on Medical Imaging*, vol. 41, no. 7, pp. 1747–1763, 2022.

[22] M. Yurt, M. Özbey, S. U. Dar, B. Tinaz, K. K. Oguz, and T. Çukur, "Progressively volumetrized deep generative models for data-efficient contextual learning of mr image recovery," *Medical Image Analysis*, vol. 78, p. 102429, 2022.

[23] L. K. Şenel, F. Şahinuç, V. Yücesoy, H. Schütze, T. Çukur, and A. Koç, "Learning interpretable word embeddings via bidirectional alignment of dimensions with semantic concepts," *Information Processing Management*, vol. 59, no. 3, p. 102925, 2022.

[24] M. Yurt, S. U. Dar, A. Erdem, E. Erdem, K. K. Oguz, and T. Çukur, "mustgan: multi-stream generative adversarial networks for mr image synthesis," *Medical Image Analysis*, vol. 70, p. 101944, 2021.

[25] S. U. Dar, M. Yurt, M. Shahdloo, M. E. Ildız, B. Tınaz, and T. Çukur, "Prior-guided image reconstruction for accelerated multi-contrast mri via generative adversarial networks," *IEEE Journal of Selected Topics in Signal Processing*, vol. 14, no. 6, pp. 1072–1087, 2020.

[26] S. U. H. Dar, M. Özbey, A. B. Çatlı, and T. Çukur, "A transfer-learning approach for accelerated mri using deep neural networks," *Magnetic Resonance in Medicine*, vol. 84, no. 2, pp. 663–685, 2020.

[27] S. U. Dar, M. Yurt, L. Karacan, A. Erdem, E. Erdem, and T. Çukur, "Image synthesis in multi-contrast mri with conditional generative adversarial networks," *IEEE Transactions on Medical Imaging*, vol. 38, no. 10, pp. 2375–2388, 2019.

[28] B. Gözcü, R. K. Mahabadi, Y.-H. Li, E. Ilıcak, T. Çukur, J. Scarlett, and V. Cevher, "Learning-based compressive mri," *IEEE Transactions on Medical Imaging*, vol. 37, no. 6, pp. 1394–1406, 2018.

[29] M. Özbey, O. Dalmaz, S. U. Dar, H. A. Bedel, Özturk, A. Güngör, and T. Çukur, "Unsupervised medical image translation with adversarial diffusion models," *IEEE Transactions on Medical Imaging*, pp. 1–1, 2023.

[30] B. Aşkın, A. Güngör, D. A. Soydan, C. B. Top, and T. Cukur, "A cnn based super-resolution technique for magnetic particle imaging system matrix," in *2021 29th Signal Processing and Communications Applications Conference (SIU)*, 2021, pp. 1–4.

[31] I. Aytekin, O. Dalmaz, H. Ankishan, E. U. Saritas, U. Bagci, T. Cukur, and H. Celik, "Detecting covid-19 from respiratory sound recordings with transformers," in *Medical Imaging 2022: Computer-Aided Diagnosis*, vol. 12033. SPIE, 2022, pp. 25–32.

[32] A. Z. Alkilani, T. Çukur, and E. U. Saritas, "Fd-net: An unsupervised deep forward-distortion model for susceptibility artifact correction in epi," *arXiv:2303.10436*, 2023.

[33] A. Güngör, B. Askin, D. A. Soydan, C. B. Top, E. U. Saritas, and T. Çukur, "Deq-mpi: A deep equilibrium reconstruction with learned consistency for magnetic particle imaging," *arXiv:2212.13233*, 2022.

[34] O. Dalmaz, B. Saglam, K. Gönç, and T. Çukur, "edagan: Encoder-decoder attention generative adversarial networks for multi-contrast mr image synthesis," in *2022 9th International Conference on Electrical and Electronics Engineering (ICEEE)*, 2022, pp. 320–324.

[35] A. Gungor, B. Aşkın, D. A. Soydan, E. U. Saritas, C. B. Top, and T. Çukur, "A denoiser scaling technique for plug-and-play mpi reconstruction," *International Journal on Magnetic Particle Imaging IJMPI*, vol. 9, no. 1 Suppl 1, 2023.

[36] F. T. Yarman Vural, S. D. Newman, T. Çukur, and I. Önal Ertugrul, "Machine learning methods for human brain imaging," *Frontiers in Neuroinformatics*, vol. 17, p. 1154835, 2023.

[37] S. Turk *et al.*, "Jointnet: A deep model for predicting active sacroiliitis from sacroiliac joint radiography," *arXiv:2301.10769*, 2023.

[38] S. U. Dar, Ş. Öztürk, M. Özbey, and T. Çukur, "Learning deep mri reconstruction models from scratch in low-data regimes," *arXiv:2301.02613*, 2023.

[39] I. Sivgin, H. A. Bedel, Ş. Öztürk, and T. Çukur, "A plug-in graph neural network to boost temporal sensitivity in fmri analysis," *arXiv:2301.00439*, 2023.

[40] M. Cemri, T. Çukur, and A. Koç, "Unsupervised simplification of legal texts," *arXiv:2209.00557*, 2022.

[41] Y. Korkmaz, M. Özbey, and T. Cukur, "Mri reconstruction with conditional adversarial transformers," in *International Workshop on Machine Learning for Medical Image Reconstruction*. Springer, 2022, pp. 62–71.

[42] B. Askin, A. Güngör, D. Alptekin Soydan, E. U. Saritas, C. B. Top, and T. Cukur, "Pp-mpi: A deep plug-and-play prior for magnetic particle imaging reconstruction," in *International Workshop on Machine Learning for Medical Image Reconstruction*. Springer, 2022, pp. 105–114.

[43] M. Acar, T. Çukur, and İ. Öksüz, "Segmentation-aware mri reconstruction," in *International Workshop on Machine Learning for Medical Image Reconstruction*. Springer, 2022, pp. 53–61.

[44] O. Dalmaz, U. Mirza, G. Elmas, M. Özbey, S. U. Dar, and T. Çukur, "A specificity-preserving generative model for federated mri translation," in *International Workshop on Distributed, Collaborative, and Federated Learning*. Springer, 2022, pp. 79–88.

[45] O. Dalmaz, U. Mirza, G. Elmas, M. Özbey, S. U. Dar, E. Ceyani, S. Avestimehr, and T. Çukur, "One model to unite them all: Personalized federated learning of multi-contrast mri synthesis," *arXiv preprint arXiv:2207.06509*, 2022.

[46] E. Ergun, A. Ö. Arol, E. U. Saritas, and T. Çukur, "A deblurring model for x-space mpi based on coded calibration scenes," *International Journal on Magnetic Particle Imaging IJMPI*, vol. 8, no. 1 Suppl 1, 2022.

[47] J. Schlemper, J. Caballero, J. V. Hajnal, A. Price, and D. Rueckert, "A Deep Cascade of Convolutional Neural Networks for MR Image Reconstruction," in *Inf Process Med Imaging*, 2017, pp. 647–658.

[48] H. K. Aggarwal, M. P. Mani, and M. Jacob, "MoDL: Model-Based deep learning architecture for inverse problems," *IEEE Trans Med Imaging*, vol. 38, no. 2, pp. 394–405, 2019.

[49] T. M. Quan, T. Nguyen-Duc, and W.-K. Jeong, "Compressed sensing MRI reconstruction with cyclic loss in generative adversarial networks," *IEEE Trans Med Imaging*, vol. 37, no. 6, pp. 1488–1497, 2018.

[50] T. Eo, Y. Jun, T. Kim, J. Jang, H.-J. Lee, and D. Hwang, "KIKI-net: cross-domain convolutional neural networks for reconstructing undersampled magnetic resonance images," *Magn Reson Med*, vol. 80, no. 5, pp. 2188–2201, 2018.

[51] M. Mardani, E. Gong, J. Y. Cheng, S. Vasanawala, G. Zaharchuk, L. Xing, and J. M. Pauly, "Deep generative adversarial neural networks for compressive sensing MRI," *IEEE Trans Med Imaging*, vol. 38, no. 1, pp. 167–179, 2019.

[52] D. Polak, S. Cauley, B. Bilgic, E. Gong, P. Bachert, E. Adalsteinsson, and K. Setsompop, "Joint multi-contrast variational network reconstruction (jVN) with application to rapid 2D and 3D imaging," *Magn Reson Med*, vol. 84, no. 3, pp. 1456–1469, 2020.

[53] S. U. Dar, M. Yurt, M. Shahdloo, M. E. Ildız, B. Tınaz, and T. Çukur, "Prior-guided image reconstruction for accelerated multi-contrast MRI via generative adversarial networks," *IEEE J Sel Topics Signal Process*, vol. 14, no. 6, pp. 1072–1087, 2020.

[54] C.-M. Feng, Z. Yang, H. Fu, Y. xu, J. Yang, and L. Shao, "Donet: Dual-octave network for fast mr image reconstruction," *IEEE Trans Neural Netw Learn Syst*, vol. PP, pp. 1–11, 07 2021.

[55] P. Guo, J. M. J. Valanarasu, P. Wang, J. Zhou, S. Jiang, and V. M. Patel, "Over-and-under complete convolutional rnn for mri reconstruction," in *Med Imaging Comput Comput Assist Interv*, 2021, pp. 13–23.

[56] D. Liang, J. Cheng, Z. Ke, and L. Ying, "Deep magnetic resonance image reconstruction: Inverse problems meet neural networks," *IEEE Signal Process Mag*, vol. 37, no. 1, pp. 141–151, 2020.

[57] G. A. Kaissis, M. R. Makowski, D. Rüeckert, and R. F. Braren, "Secure, privacy-preserving and federated machine learning in medical imaging," *Nat. Mach. Intell.*, vol. 2, no. 6, pp. 305–311, 2020.

[58] W. Li *et al.*, "Privacy-preserving federated brain tumour segmentation," in *Mach Learn Med Imaging*, 2019, pp. 133–141.

[59] M. J. Sheller, G. A. Reina, B. Edwards, J. Martin, and S. Bakas, "Multi-institutional deep learning modeling without sharing patient data: A feasibility study on brain tumor segmentation," in *Med Imaging Comput Comput Assist Interv*, 2019, pp. 92–104.

[60] N. Rieke *et al.*, "The future of digital health with federated learning," *NPJ Digit Med*, vol. 3, no. 1, p. 119, 2020.

[61] H. R. Roth *et al.*, "Federated Learning for Breast Density Classification: A Real-World Implementation," in *Dom Adapt Rep Trans*, 2020, p. 181–191.

[62] X. Li, Y. Gu, N. Dvornek, L. H. Staib, P. Ventola, and J. S. Duncan, "Multi-site fmri analysis using privacy-preserving federated learning and domain adaptation: Abide results," *Med Image Anal*, vol. 65, p. 101765, 2020.

[63] Q. Liu, C. Chen, J. Qin, Q. Dou, and P. Heng, "Feddg: Federated domain generalization on medical image segmentation via episodic learning in continuous frequency space," in *Comput Vis Pattern Recognit*, 2021, pp. 1013–1023.

[64] H. B. McMahan, E. Moore, D. Ramage, S. Hampson, and B. A. y Arcas, "Communication-efficient learning of deep networks from decentralized data," in *Int Conf Artif Intell Stat*, 2017.

[65] J. Wang *et al.*, "A field guide to federated optimization," *arXiv:2107.06917*, 2021.

[66] T. Li, A. K. Sahu, A. S. Talwalkar, and V. Smith, "Federated learning: Challenges, methods, and future directions," *IEEE Signal Process Mag*, vol. 37, pp. 50–60, 2020.

[67] D. Narnhofer, K. Hammernik, F. Knoll, and T. Pock, "Inverse GANs for accelerated MRI reconstruction," in *SPIE Med Imaging*, vol. 11138, 2019, pp. 381 – 392.

[68] F. Knoll *et al.*, "fastMRI: A publicly available raw k-space and DICOM dataset of knee images for accelerated MR image reconstruction using machine learning," *Rad Artif Intell*, vol. 2, no. 1, p. e190007, 2020.

[69] F. Knoll, K. Hammernik, E. Kobler, T. Pock, M. P. Recht, and D. K. Sodickson, "Assessment of the generalization of learned image reconstruction and the potential for transfer learning," *Magn Reson Med*, vol. 81, no. 1, pp. 116–128, 2019.

[70] P. Guo, P. Wang, J. Zhou, S. Jiang, and V. M. Patel, "Multi-institutional Collaborations for Improving Deep Learning-based Magnetic Resonance Image Reconstruction Using Federated Learning," *arXiv:2103.02148*, 2021.

[71] C.-M. Feng, Y. Yan, S. Wang, Y. Xu, L. Shao, and H. Fu, "Specificity-Preserving Federated Learning for MR Image Reconstruction," *arXiv:2112.05752*, 2021.

[72] B. Zhu, J. Z. Liu, B. R. Rosen, and M. S. Rosen, "Image reconstruction by domain transform manifold learning," *Nature*, vol. 555, no. 7697, pp. 487–492, 2018.

[73] S. Biswas, H. K. Aggarwal, and M. Jacob, "Dynamic MRI using model-based deep learning and SToRM priors: MoDL-SToRM," *Magn Reson Med*, vol. 82, no. 1, pp. 485–494, 2019.

[74] Q. Chang, H. Qu, Y. Zhang, M. Sabuncu, C. Chen, T. Zhang, and D. N. Metaxas, "Synthetic learning: Learn from distributed asynchronized discriminator GAN without sharing medical image data," in *Comput Vis Pattern Recognit*, 2020, pp. 13 853–13 863.

[75] P. Guo, P. Wang, R. Yasarla, J. Zhou, V. M. Patel, and S. Jiang, "Anatomic and molecular mr image synthesis using confidence guided cnns," *IEEE Trans Med Imaging*, vol. 40, no. 10, pp. 2832–2844, 2021.

[76] G. Oh, B. Sim, H. Chung, L. Sunwoo, and J. C. Ye, "Unpaired deep learning for accelerated MRI using optimal transport driven cycleGAN," *IEEE Trans Comput Imaging*, vol. 6, pp. 1285–1296, 2020.

[77] K. Lei, M. Mardani, J. M. Pauly, and S. S. Vasanawala, "Wasserstein gans for mr imaging: From paired to unpaired training," *IEEE Trans Med Imaging*, vol. 40, no. 1, pp. 105–115, 2021.

[78] B. Yaman, S. A. H. Hosseini, S. Moeller, J. Ellermann, K. Ugurbil, and M. Akcakaya, "Self-supervised learning of physics-guided reconstruction neural networks without fully sampled reference data," *Magn Reson Med*, vol. 84, no. 6, pp. 3172–3191, 2020.

[79] P. Huang, C. H. Li, S. K. Gaire, R. Liu, X. Zhang, X. Li, and L. Ying, "Deep MRI reconstruction without ground truth for training," in *Int Soc Magn Reson Med*, 2019, p. 4668.

[80] J. I. Tamir, S. X. Yu, and M. Lustig, "Unsupervised deep basis pursuit: Learning reconstruction without ground-truth data," in *Int Soc Magn Reson Med*, 2019, p. 0660.

[81] C. Hu, C. Li, H. Wang, Q. Liu, H. Zheng, and S. Wang, "Self-supervised Learning for MRI Reconstruction with a Parallel Network Training Framework," in *Med Imaging Comput Comput Assist Interv.* Cham: Springer, 2021, pp. 382–391.

[82] F. Liu, R. Kijowski, G. El Fakhri, and L. Feng, "Magnetic resonance parameter mapping using model-guided self-supervised deep learning," *Magn Reson Med*, vol. 85, no. 6, pp. 3211–3226, 2021.

[83] S. Wang, R. Wu, C. Li, J. Zou, X. Liu, Q. Liu, Y. Xi, and H. Zheng, "PARCEL: Physics-based unsupervised contrastive representation learning for parallel MR imaging," *arXiv:2202.01494*, 2022.

[84] S. Cetin Karayumak, S. Bouix, L. Ning, A. James, T. Crow, M. Shenton, M. Kubicki, and Y. Rathi, "Retrospective harmonization of multi-site diffusion mri data acquired with different acquisition parameters," *NeuroImage*, vol. 184, pp. 180–200, 2019.

[85] B. E. Dewey *et al.*, "Deepharmony: A deep learning approach to contrast harmonization across scanner changes," *Magn Reson Imaging*, vol. 64, pp. 160–170, 2019.

[86] X. Li, M. Jiang, X. Zhang, M. Kamp, and Q. Dou, "FedBN: Federated learning on non-IID features via local batch normalization," in *Int Conf Learn Rep*, 2021.

[87] Z. Yan, J. Wicaksana, Z. Wang, X. Yang, and K.-T. Cheng, "Variation-aware federated learning with multi-source decentralized medical image data," *IEEE J. Biomed. Health Inform.*, vol. 25, no. 7, pp. 2615–2628, 2021.

[88] S. Park, G. Kim, J. Kim, B. Kim, and J. C. Ye, "Federated Split Task-Agnostic Vision Transformer for COVID-19 CXR Diagnosis," in *Adv Neural Inf Process Syst*, 2021.

[89] K. C. Tezcan, C. F. Baumgartner, R. Luechinger, K. P. Pruessmann, and E. Konukoglu, "MR image reconstruction using deep density priors," *IEEE Trans Med Imaging*, vol. 38, no. 7, pp. 1633–1642, 2019.

[90] Y. Korkmaz, S. U. Dar, M. Yurt, M. Özbey, and T. Çukur, "Unsupervised MRI Reconstruction via Zero-Shot Learned Adversarial Transformers," *IEEE Trans Med Imaging*, vol. 41, no. 7, pp. 1747–1763, 2022.

[91] O. B. Demirel, T. Kilic, T. Çukur, and E. U. Saritas, "Anatomical measurements correlate with individual magnetostimulation thresholds for khz-range homogeneous magnetic fields," *Medical Physics*, vol. 47, no. 4, pp. 1836–1844, 2020.

[92] M. Shahdloo, E. Ilicak, M. Tofighi, E. U. Saritas, A. E. Çetin, and T. Çukur, "Projection onto epigraph sets for rapid self-tuning compressed sensing mri," *IEEE Transactions on Medical Imaging*, vol. 38, no. 7, pp. 1677–1689, 2019.

[93] T. Cukur, J. M. Santos, J. M. Pauly, and D. G. Nishimura, "Variable-density parallel imaging with partially localized coil sensitivities," *IEEE Transactions on Medical Imaging*, vol. 29, no. 5, pp. 1173–1181, 2010.

[94] E. Biyik, E. Ilicak, and T. Çukur, "Reconstruction by calibration over tensors for multi-coil multi-acquisition balanced ssfp imaging," *Magnetic Resonance in Medicine*, vol. 79, no. 5, pp. 2542–2554, 2018.

[95] E. Ilicak, L. K. Senel, E. Biyik, and T. Çukur, "Profile-encoding reconstruction for multiple-acquisition balanced steady-state free precession imaging," *Magnetic Resonance in Medicine*, vol. 78, no. 4, pp. 1316–1329, 2017.

[96] E. Kopanoglu, A. Güngör, T. Kilic, E. U. Saritas, K. K. Oguz, T. Çukur, and H. E. Güven, "Simultaneous use of individual and joint regularization terms in compressive sensing: Joint reconstruction of multi-channel multi-contrast mri acquisitions," *NMR in Biomedicine*, vol. 33, no. 4, p. e4247, 2020, e4247 NBM-19-0101.R2.

[97] L. K. Senel, T. Kilic, A. Gungor, E. Kopanoglu, H. E. Guven, E. U. Saritas, A. Koc, and T. Çukur, "Statistically segregated k-space sampling for accelerating multiple-acquisition mri," *IEEE Transactions on Medical Imaging*, vol. 38, no. 7, pp. 1701–1714, 2019.

[98] E. Ilicak, S. Cetin, E. Bulut, K. K. Oguz, E. U. Saritas, G. Unal, and T. Çukur, "Targeted vessel reconstruction in non-contrast-enhanced steady-state free precession angiography," *NMR in Biomedicine*, vol. 29, no. 5, pp. 532–544, 2016.

[99] T. Çukur, "Accelerated phase-cycled ssfp imaging with compressed sensing," *IEEE Transactions on Medical Imaging*, vol. 34, no. 1, pp. 107–115, 2015.

[100] T. Çukur, M. Lustig, E. U. Saritas, and D. G. Nishimura, "Signal compensation and compressed sensing for magnetization-prepared mr angiography," *IEEE Transactions on Medical Imaging*, vol. 30, no. 5, pp. 1017–1027, 2011.

[101] D. J. Holland, C. Liu, X. Song, E. L. Mazerolle, M. T. Stevens, A. J. Sederman, L. F. Gladden, R. C. N. D'Arcy, C. V. Bowen, and S. D. Beyea, "Compressed sensing reconstruction improves sensitivity of variable density spiral fmri," *Magnetic Resonance in Medicine*, vol. 70, no. 6, pp. 1634–1643, 2013.

[102] T. Çukur, M. Lustig, and D. G. Nishimura, "Improving non-contrast-enhanced steady-state free precession angiography with compressed sensing," *Magnetic Resonance in Medicine*, vol. 61, no. 5, pp. 1122–1131, 2009.

[103] T. Cukur, J. H. Lee, N. K. Bangerter, B. A. Hargreaves, and D. G. Nishimura, "Non-contrast-enhanced flow-independent peripheral MR angiography with balanced SSFP," *Magn. Reson. Med.*, vol. 61, no. 6, pp. 1533–1539, Jun. 2009.

[104] T. Cukur and D. G. Nishimura, "Multiple repetition time balanced steady-state free precession imaging," *Magn. Reson. Med.*, vol. 62, no. 1, pp. 193–204, Jul. 2009.

[105] T. Çukur, M. Lustig, and D. G. Nishimura, "Multiple-profile homogeneous image combination: Application to phase-cycled ssfp and multicoil imaging," *Magnetic Resonance in Medicine*, vol. 60, no. 3, pp. 732–738, 2008.

[106] T. Çukur, N. K. Bangerter, and D. G. Nishimura, "Enhanced spectral shaping in steady-state free precession imaging," *Magnetic Resonance in Medicine*, vol. 58, no. 6, pp. 1216–1223, 2007.

[107] B. Gozcu, R. K. Mahabadi, Y.-H. Li, E. Ilicak, T. Cukur, J. Scarlett, and V. Cevher, "Learning-based compressive mri," *IEEE transactions on medical imaging*, vol. 37, no. 6, p. 1394—1406, June 2018.

[108] A. Güngör, E. Kopanoğlu, T. Çukur, and H. E. Güven, "Compressed multi-contrast magnetic resonance image reconstruction using augmented lagrangian method," in *2016 24th Signal Processing and Communication Application Conference (SIU)*, 2016, pp. 1985–1988.

[109] A. Güngör, E. Kopanoglu, T. Cukur, and H. E. Güven, "A synthesis-based approach to compressive multi-contrast magnetic resonance imaging," in *2017 IEEE 14th International Symposium on Biomedical Imaging (ISBI 2017)*, 2017, pp. 696–699.

[110] A. Koc, H. M. Ozaktas, B. Bartan, E. Gundogdu, and T. Cukur, "Digital computation of fractional fourier and linear canonical transforms and sparse image representation," in *2017 Asia-Pacific Signal and Information Processing Association Annual Summit and Conference (APSIPA ASC)*, 2017, pp. 111–117.

[111] P. Aggarwal and A. Gupta, "Accelerated fmri reconstruction using matrix completion with sparse recovery via split bregman," *Neurocomputing*, vol. 216, pp. 319–330, 2016.

[112] T. Kılıç, T. Çukur, O. Algın, and E. Sarıtaş, "Joint partial fourier and compressed sensing reconstruction for accelerated time-of-flight mr angiography," in *2018 26th Signal Processing and Communications Applications Conference (SIU)*, 2018, pp. 1–4.

[113] M. Aksoy, C. Forman, M. Straka, T. Çukur, J. Hornegger, and R. Bammer, "Hybrid prospective and retrospective head motion correction to mitigate cross-calibration errors," *Magnetic Resonance in Medicine*, vol. 67, no. 5, pp. 1237–1251, 2012.

[114] A. Güngör, E. Kopanoğlu, T. Çukur, and H. E. Güven, "Fast recovery of compressed multi-contrast magnetic resonance images," in *Medical Imaging 2017: Image Processing*, M. A. Styner and E. D. Angelini, Eds., vol. 10133, International Society for Optics and Photonics. SPIE, 2017, p. 101331R.

[115] T. Çukur, "Spectrally selective imaging with wideband balanced steady-state free precession mri," *Magnetic Resonance in Medicine*, vol. 75, no. 3, pp. 1132–1141, 2016.

[116] T. Cukur, J. M. Santos, J. M. Pauly, and D. G. Nishimura, "Variable-density parallel imaging with partially localized coil sensitivities," *IEEE Trans. Med. Imaging*, vol. 29, no. 5, pp. 1173–1181, May 2010.

[117] A. Koç, B. Bartan, E. Gundogdu, T. Çukur, and H. M. Ozaktas, "Sparse representation of two- and three-dimensional images with fractional fourier, hartley, linear canonical, and haar wavelet transforms," *Expert Systems with Applications*, vol. 77, pp. 247–255, 2017.

[118] U. Gamper, P. Boesiger, and S. Kozerke, "Compressed sensing in dynamic mri," *Magnetic Resonance in Medicine*, vol. 59, no. 2, pp. 365–373, 2008.

[119] T. Çukur, J. M. Santos, D. G. Nishimura, and J. M. Pauly, "Varying kernel-extent gridding reconstruction for undersampled variable-density spirals," *Magnetic Resonance in Medicine*, vol. 59, no. 1, pp. 196–201, 2008.

[120] B. Quist, B. A. Hargreaves, T. Cukur, G. R. Morrell, G. E. Gold, and N. K. Bangerter, "Simultaneous fat suppression and band reduction with large-angle multiple-acquisition balanced steady-state free precession," *Magnetic Resonance in Medicine*, vol. 67, no. 4, pp. 1004–1012, 2012.

[121] S. Ilbey, C. Top, A. Güngör, T. Cukur, E. Saritas, and H. Guven, "Comparison of system-matrix-based and projection-based reconstructions for field free line magnetic particle imaging," *International Journal on Magnetic Particle Imaging*, vol. 3, 01 2017.

[122] B. Bilgic, V. Goyal, and E. Adalsteinsson, "Multi-contrast reconstruction with bayesian compressed sensing," *Magnetic resonance in medicine : official journal of the Society of Magnetic Resonance in Medicine / Society of Magnetic Resonance in Medicine*, vol. 66, pp. 1601–15, 12 2011.

[123] C. Furkan Senel and T. Cukur, "Variable-fov reconstruction for 3d non-cartesian parallel imaging," in *2017 21st National Biomedical Engineering Meeting (BIYOMUT)*, 2017, pp. i–iii.

[124] A. Gungor, E. Kopanoglu, T. Cukur, E. Guven, and F. T. Yarman-Vural, "Joint dictionary learning reconstruction of compressed multi-contrast magnetic resonance imaging," in *2017 21st National Biomedical Engineering Meeting (BIYOMUT)*, 2017, pp. i–iv.

[125] J. P. Haldar, D. Hernando, and Z.-P. Liang, "Compressed-sensing mri with random encoding," *IEEE Transactions on Medical Imaging*, vol. 30, no. 4, pp. 893–903, 2011.

[126] E. Ilıcak and T. Çukur, "Ruber function based reconstruction in accelerated phase-cycled bssfp acquisitions for increased detection performance," in *2017 25th Signal Processing and Communications Applications Conference (SIU)*, 2017, pp. 1–4.

[127] Y. B. Can, E. Ilıcak, and T. Çukur, "Fast 3d variable-fov reconstruction for parallel imaging with localized sensitivities," *arXiv:1612.00157*, 2016.

[128] E. Ilicak, S. Cetin, E. U. Saritas, G. Unal, and T. çukur, "Adaptive reconstruction for vessel preservation in unenhanced mr angiography," in *2016 24th Signal Processing and Communication Application Conference (SIU)*, 2016, pp. 577–580.

[129] Yılmaz, E. Sarıtaş, and T. Çukur, "Phase-sensitive reconstruction for fat-water separation in multi-coil acquisitions," in *2016 24th Signal Processing and Communication Application Conference (SIU)*, 2016, pp. 469–472.

[130] M. Lustig, D. Donoho, and J. M. Pauly, "Sparse mri: The application of compressed sensing for rapid mr imaging," *Magnetic Resonance in Medicine*, vol. 58, no. 6, pp. 1182–1195, 2007.

[131] S. Ma, W. Yin, Y. Zhang, and A. Chakraborty, "An efficient algorithm for compressed mr imaging using total variation and wavelets," in *2008 IEEE Conference on Computer Vision and Pattern Recognition*, 2008, pp. 1–8.

[132] K. H. Jin, D. Lee, and J. C. Ye, "A general framework for compressed sensing and parallel mri using annihilating filter based low-rank hankel matrix," *IEEE Transactions on Computational Imaging*, vol. 2, no. 4, pp. 480–495, 2016.

[133] X. Zhang, D. Guo, Y. Huang, Y. Chen, L. Wang, F. Huang, Q. Xu, and X. Qu, "Image reconstruction with low-rankness and self-consistency of k-space data in parallel mri," *Medical Image Analysis*, vol. 63, p. 101687, 2020.

[134] E. Ilicak, E. U. Saritas, and T. Çukur, "Automated parameter selection for accelerated mri reconstruction via low-rank modeling of local k-space neighborhoods," *Zeitschrift für Medizinische Physik*, 2022.

[135] J. P. Haldar, "Low-rank modeling of local k-space neighborhoods (loraks) for constrained mri," *IEEE Transactions on Medical Imaging*, vol. 33, no. 3, pp. 668–681, 2014.

[136] M. Özbey and T. Çukur, "Multi-image reconstruction in multi-contrast mri," in *2021 29th Signal Processing and Communications Applications Conference (SIU)*, 2021, pp. 1–4.

[137] Kaftan, v. B. Gevrek, and T. Çukur, "Synergistic reconstruction-synthesis of multi-contrast mri using transfer learning method," in *2021 29th Signal Processing and Communications Applications Conference (SIU)*, 2021, pp. 1–4.

[138] S. U. H. Dar, M. Yurt, and T. Çukur, "A few-shot learning approach for accelerated mri via fusion of data-driven and subject-driven priors," *arXiv:2103.07790*, 2021.

[139] M. Özbey, M. Yurt, S. U. H. Dar, and T. Çukur, "Three dimensional mr image synthesis with progressive generative adversarial networks," *arXiv:2101.05218*, 2020.

[140] M. Acar, T. Çukur, and İ. Öksüz, "Self-supervised dynamic mri reconstruction," in *Machine Learning for Medical Image Reconstruction*, N. Haq, P. Johnson, A. Maier, T. Würfl, and J. Yoo, Eds. Cham: Springer International Publishing, 2021, pp. 35–44.

[141] S. U. H. Dar, M. Yurt, M. Shahdloo, M. E. Ildız, and T. Çukur, "Synergistic reconstruction and synthesis via generative adversarial networks for accelerated multi-contrast mri," *arXiv:1805.10704*, 2018.

[142] M. Pandey, M. Fernandez, F. Gentile, O. Isayev, A. Tropsha, A. C. Stern, and A. Cherkasov, "The transformational role of gpu computing and deep learning in drug discovery," *Nature Machine Intelligence*, vol. 4, no. 3, pp. 211–221, Mar 2022.

[143] G. Huang, Z. Liu, L. Van Der Maaten, and K. Q. Weinberger, "Densely connected convolutional networks," in *2017 IEEE Conference on Computer Vision and Pattern Recognition (CVPR)*, 2017, pp. 2261–2269.

[144] A. Dosovitskiy *et al.*, "An image is worth 16x16 words: Transformers for image recognition at scale," *arXiv:2010.11929*, 2020.

[145] D. Killock, "Ai outperforms radiologists in mammographic screening," *Nature Reviews Clinical Oncology*, vol. 17, no. 3, pp. 134–134, Mar 2020.

[146] G. Kaissis *et al.*, "End-to-end privacy preserving deep learning on multi-institutional medical imaging," *Nature Machine Intelligence*, vol. 3, no. 6, pp. 473–484, Jun 2021.

[147] M. A. Bansal, D. R. Sharma, and D. M. Kathuria, "A systematic review on data scarcity problem in deep learning: Solution and applications," *ACM Comput. Surv.*, vol. 54, no. 10s, sep 2022.

[148] J. Lever, M. Krzywinski, and N. Altman, "Model selection and overfitting," *Nature Methods*, vol. 13, no. 9, pp. 703–704, Sep 2016.

[149] M. J. Sheller *et al.*, "Federated learning in medicine: facilitating multi-institutional collaborations without sharing patient data," *Scientific Reports*, vol. 10, no. 1, p. 12598, Jul 2020.

[150] R. VanRullen and L. Reddy, "Reconstructing faces from fmri patterns using deep generative neural networks," *Communications Biology*, vol. 2, no. 1, p. 193, May 2019.

[151] A. B. Mansour, G. Carenini, A. Duplessis, and D. Naccache, "Federated learning aggregation: New robust algorithms with guarantees," in *2022 21st IEEE International Conference on Machine Learning and Applications (ICMLA)*, 2022, pp. 721–726.

[152] T. Karras, S. Laine, and T. Aila, "A style-based generator architecture for generative adversarial networks," in *Comput Vis Pattern Recognit*, 2019, pp. 4401–4410.

[153] X. Huang and S. J. Belongie, "Arbitrary style transfer in real-time with adaptive instance normalization," *arXiv:1703.06868*, 2017.

[154] M. Uecker, P. Lai, M. J. Murphy, P. Virtue, M. Elad, J. M. Pauly, S. S. Vasanawala, and M. Lustig, "ESPIRiT-an eigenvalue approach to autocalibrating parallel MRI: Where SENSE meets GRAPPA," *Magn Reson Med*, vol. 71, no. 3, pp. 990–1001, 2014.

[155] H. K. Aggarwal and M. Jacob, "Model adaptation for image reconstruction using generalized Stein's unbiased risk estimator," *arXiv:2102.00047*, 2021.

[156] J. P. Haldar and J. Zhuo, "P-LORAKS: Low-Rank Modeling of Local k-Space Neighborhoods with Parallel Imaging Data," *Magn Reson Med*, vol. 75, no. 4, p. 1499, 2016.

[157] M. Rasouli, T. Sun, and R. Rajagopal, "Fedgan: Federated generative adversarial networks for distributed data," *arXiv:2006.07228*, 2020.

[158] P. P. Liang, T. Liu, L. Ziyin, N. B. Allen, R. P. Auerbach, D. Brent, R. Salakhutdinov, and L.-P. Morency, "Think locally, act globally: Federated learning with local and global representations," *arXiv:2001.01523*, 2020.

[159] B. H. Menze *et al.*, "The multimodal brain tumor image segmentation benchmark (brats)," *IEEE Trans Med Imaging*, vol. 34, no. 10, pp. 1993–2024, 2015.

[160] T. Zhang, J. M. Pauly, S. S. Vasanawala, and M. Lustig, "Coil compression for accelerated imaging with Cartesian sampling." *Magn Reson Med*, vol. 69, no. 2, pp. 571–82, 2013.

[161] D. Chen, N. Yu, Y. Zhang, and M. Fritz, "GAN-Leaks: A Taxonomy of Membership Inference Attacks against Generative Models," in *SIGSAC Conf Comput Commun Sec.* USA: ACM, 2020, p. 343–362.

[162] M. Murphy, M. Alley, J. Demmel, K. Keutzer, S. Vasanawala, and M. Lustig, "Fast ℓ_1 -SPIRiT Compressed Sensing Parallel Imaging MRI: Scalable Parallel Implementation and Clinically Feasible Runtime," *IEEE Trans Med Imaging*, vol. 31, no. 6, pp. 1250–1262, 2012.

[163] Q. Feng, C. Guo, F. Benitez-Quiroz, and A. Martinez, "When do GANs replicate? on the choice of dataset size," in *Int Conf Comput Vis*, 2021, pp. 6701–6710.

[164] T. Han, S. Nebelung, C. Haarburger, N. Horst, S. Reinartz, D. Merhof, F. Kiessling, V. Schulz, and D. Truhn, "Breaking medical data sharing boundaries by using synthesized radiographs," *Sci Adv*, vol. 6, no. 49, p. eabb7973, 2020.

[165] L. Zhang, B. Shen, A. Barnawi, S. Xi, N. Kumar, and Y. Wu, "FedDPGAN: Federated Differentially Private Generative Adversarial Networks Framework for the Detection of COVID-19 Pneumonia," *Inf Syst Front*, vol. 23, no. 6, pp. 1403–1415, 2021.

[166] A. Ziller, D. Usynin, M. Knolle, K. Hammernik, D. Rueckert, and G. Kaissis, "Complex-valued deep learning with differential privacy," *arXiv:2110.03478*, 2021.

[167] M. Zhang, K. Sapra, S. Fidler, S. Yeung, and J. M. Alvarez, "Personalized federated learning with first order model optimization," in *Int Conf Learn Rep*, 2021.

[168] X. Ma, J. Zhang, S. Guo, and W. Xu, "Layer-wised model aggregation for personalized federated learning," *arXiv:2205.03993*, 2022.